

**REMOTE SENSING STUDY OF SÜRGÜ FAULT ZONE  
(MALATYA, TURKEY)**

**A THESIS SUBMITTED TO  
THE GRADUATE SCHOOL OF NATURAL AND APPLIED SCIENCES  
OF  
MIDDLE EAST TECHNICAL UNIVERSITY**

**BY**

**AYTEN KOÇ**

**IN PARTIAL FULFILLMENT OF THE REQUIREMENTS  
FOR  
THE DEGREE OF MASTER OF SCIENCE  
IN  
GEODETIC AND GEOGRAPHICAL INFORMATION TECHNOLOGIES**

**SEPTEMBER 2005**

Approval of the Graduate School of Natural and Applied Sciences

---

Prof. Dr. Canan Özgen  
Director

I certify that this thesis satisfies all the requirements as a thesis for the degree of Master of Science.

---

Assist. Prof. Dr. Zuhal Akyürek  
Head of Department

This is to certify that we have read this thesis and that in our opinion it is fully adequate, in scope and quality, as a thesis for the degree of Master of Science.

---

Assist. Prof. Dr. Nuretdin Kaymakçı  
Supervisor

Examining Committee Members

Prof. Dr. Vedat TOPRAK (METU, GEOE) \_\_\_\_\_

Assist. Prof. Dr. Nuretdin KAYMAKÇI (METU, GEOE) \_\_\_\_\_

Assoc. Prof. Dr. Bora ROJAY (METU, GEOE) \_\_\_\_\_

Assist. Prof. Dr. Zuhal AKYÜREK (METU, GGIT) \_\_\_\_\_

Assist. Prof. Dr. Lütfi SÜZEN (METU, GEOE) \_\_\_\_\_

**I hereby declare that all information in this document has been obtained and presented in accordance with academic rules and ethical conduct. I also declare that, as required by these rules and conduct, I have fully cited and referenced all material and results that are not original to this work.**

Name, Last Name: Ayten Koç

Signature:

## **ABSTRACT**

### REMOTE SENSING STUDY OF SÜRGÜ FAULT ZONE (MALATYA, TURKEY)

KOÇ, Ayten

M. Sc., Geodetic and Geographic Information Technologies  
Supervisor: Assist. Prof. Dr. Nuretdin Kaymakçı

September 2005, 90 pages

The geometry, deformation mechanism and kinematics of the Sürgü Fault Zone is investigated by using remotely sensed data including Landsat TM and ASTER imagery combined with SRTM, and stereo-aerial photographs. They are used to extract information related to regional lineaments and tectono-morphological characteristics of the SFZ. Various image processing and enhancement techniques including contrast enhancement, PCA, DS and color composites are applied on the imagery and three different approaches including manual, semi automatic and automatic lineament extraction methods are followed. Then the lineaments obtained from ASTER and Landsat imagery using manual and automatic methods are overlaid to produce a final lineaments map.

The results have indicated that, the total number and length of the lineaments obtained from automatic is more than other methods while the percentages of overlapping lineaments for the manual method is more than the automatic method which indicate that the lineaments from automatic method does not discriminate man made features which result more lineaments and less overlapping ratio with respect to final map.

It is revealed from the detail analysis that, the SFZ displays characteristic deformation patterns of strike-slip faults, such as pressure ridges, linear fault controlled valleys, deflected stream courses, rotated blocks and juxtaposition of stratigraphical horizons in macroscopic scale. In addition to these, kinematic analyses carried out using fault slip data indicated that the Sürgü Fault Zone is dextral strike-slip fault zone with a reverse component of slip and cumulative displacement along the fault is more than 2 km.

**Keywords:** Sürgü Fault Zone, Dextral Strike-Slip Fault Zone, Satellite Remote Sensing, Aerial Photographs, Kinematics.

## ÖZ

### SÜRGÜ FAY ZONUNUN UZAKTAN ALGILAMA İ İLE ÇALIŞILMASI (MALATYA, TÜRKİYE)

KOÇ, Ayten

Yüksek Lisans, Jeodezi ve Coğrafi Bilgi Teknolojileri Anabilim Dalı

Tez Yöneticisi: Yrd. Doç. Dr. Nuretdin Kaymakçı

September 2005, 90 sayfa

Bu çalışmada, Landsat TM, ASTER ile birlikte Shuttle Radar Topography Mission'dan elde edilen Sayısal Yükseklik Modeli ve stereo-hava fotoğrafları kullanılarak Sürgü Fay Kuşağının (SFK) geometrisi, deformasyon mekanizması ve kinematikleri araştırılmıştır. Bu veri setleri, bölgesel çizgiselliklerle ilişkili bilgilerin ve SFK'nın tektono-morfolojik karakteristiğinin çıkarılması amacı ile kullanılmıştır. Çeşitli görüntü işleme ve Kontrast iyileştirme, temel bileşen analizi, dekorelasyon analizi ve renk kombinasyonları gibi görüntü iyileştirme teknikleri kullanılmış, el ile, yarı-otomatik ve otomatik olmak üzere üç değişik yaklaşım çizgisellikleri belirlemek amacı ile kullanılmıştır. Daha sonra otomatik olmayan (el ile) ve otomatik yöntemler ile ASTER ve Landsat TM görüntülerinden elde edilen çizgisellikler üst üste karşılaştırılarak sonuç çizgisellik haritası elde edilmiştir.

Sonuçlar göstermiştir ki, otomatik yöntem ile elde edilen çizgiselliklerin sayısı ve toplam uzunluğu diğer yaklaşımlar kullanılarak elde edilenlerden daha fazla olmasına karşın otomatik olmayan yöntem için çakışan çizgiselliklerin yüzdesi otomatik yöntemlere göre daha yüksektir. Bu durum otomatik yöntemlerin insan etkisi ile oluşmuş çizgisel yapıların ayırt edemediğini göstermiştir ki, çok sayıda çizgisellik belirlenmesi ve az oranda çakışmanın olması bu durumun sonucudur.

Yapılan detaylı analizler göstermiştir ki, SFK büyük ölçekte doğrultu atımlı faylarda ortak olan deformasyon yapıları göstermektedir, örneğin; basınç sırtları, fay kontrollü çizgisel vadiler, ötelenmiş nehir yatakları, dönmüş bloklar ve uyumsuz stratigrafik birimler gibi. Yukarda bahsedilen özelliklere ek olarak, fay kayma verileri kullanılarak yapılan kinematik analizler göstermektedir ki SFK ters kayma birleşenli sağ yanal doğrultu-atımlı bir fay kuşağıdır ve fay boyunca birimli yer değiştirme 2 km'den fazladır.

**Anahtar Kelimeler:** Sürgü Fay Zonu, Sağ Yanal Doğrultu Atımlı Fay Kuşağı, Uydudan Uzaktan Algılama, Hava Fotoğrafları, Kinematik.

**This work is dedicated to my family**

## ACKNOWLEDGEMENTS

First, thanks and praise to God, who freely and lovingly gave the strength, motivation, wisdom and encouragement to see me through the difficult times.

Many people have contributed to this thesis, and to the editing process. Were it not for the aid, support and encouragement of these people, this thesis would not be what it is. I would like to express my sincere gratefulness; nevertheless I know that the words are not enough to express their contributions and support.

Among all, I would like to thank to my supervisor, Assist. Prof Dr. Nuretdin Kaymakçı, for his wisdom, insight, guidance, motivation, kindness and continuous support in every stage of this thesis. He was always giving me strength to continue my work in a friendly, open and kind manner. He is more than a supervisor for me. I have to say that I learned a lot of things that are not only related to this thesis but also daily life from him. Thank you “*hocam*”, I hope every M. Sc. and Ph. D. student would have a supervisor like you. Working with you was and will be a great pleasure for me.

Thanks to Prof. Dr. Vedat Toprak, Assoc. Prof. Dr. Bora Rojay, and Assist. Prof. Dr. Lütfi Süzen for their comments and assistance which have enabled me to visualize the related concepts and aspects more effectively.

I would like to express my sincere gratitude to Mahmut Arıkan who was cheering me up and giving me strength when I was discouraged and depressed. We shared the good time, bad time and the time in between ☺. Besides, I would also like to thank him for his contribution to my skills and knowledge which in turn ease my tasks. Thank you Mahmut, I could not overcome my hard days without you. I will miss you very much when you are far from me!

I would like to thank also to all friends in RS-GIS lab, especially Deniz Gerçek, Başak Şener and Alper Fulat, who helped me to overcome the problems about

TNT Mips, also for the joyful time we shared and to Pınar Ertepinar, for help during field work and her kind hospitality during my studies.

I would like to express my gratitude to all friends in GGIT, especially Arzu Erener who is my cellmate in GGIT for her friendship and kind manner.

I would like to express my sincere feelings to my old friends Esra and Kubra twins to whom I have shared most of the amusing time at my home town Fatsa.

I would like to thank my sisters, Fatma, Aysegül, Aysel and my brothers, Kemal and Hasan for their unlimited patience and continuous support (financial and moral), not only in this study but also throughout my whole life. Especially, my sister Aysegül are more than a sister to me. I always see my mother on her face. I love all of you very much!

Last, but not least, I would like to thank my parents, Huriye and Necmettin, who imparted in me the confidence to pursue my personal goals, even when this pursuit led us to a place so far from home.

This research was supported by ÖYP research foundation No: BAP-08-11-DPT.2002K120510

# TABLE OF CONTENTS

|                                |        |
|--------------------------------|--------|
| <b>PLAGIARISM</b> .....        | iii    |
| <b>ABSTRACT</b> .....          | iv     |
| <b>ÖZ</b> .....                | vi     |
| <b>DEDICATION</b> .....        | viii   |
| <b>ACKNOWLEDGMENTS</b> .....   | ix     |
| <b>TABLE OF CONTENTS</b> ..... | xi     |
| <b>LIST OF TABLES</b> .....    | xix    |
| <b>LIST OF FIGURES</b> .....   | xivx   |
| <b>ABBREVIATIONS</b> .....     | xviiix |

## CHAPTER

|  |    |
|--|----|
| <b>1. INTRODUCTION</b> .....                               | 1  |
| 1.1 Purpose and Scope .....                                | 1  |
| 1.2 Study Area .....                                       | 3  |
| 1.3 Method and Context of the Study .....                  | 5  |
| 1.4 Previous Studies .....                                 | 6  |
| 1.4.1 Studies Related to Remote Sensing .....              | 6  |
| 1.4.2 Studies Related to Geology of the Region .....       | 10 |
| <b>2. REMOTE SENSING AND LINEAMENT DELINIATION</b> .....   | 13 |
| 2.1 Definition of Lineament .....                          | 13 |
| 2.2 Enhancement Techniques for Lineament Delineation ..... | 14 |
| 2.2.1 Contrast Enhancement .....                           | 14 |
| 2.2.2 Color Composite .....                                | 15 |
| 2.2.3 Principle Component Analysis .....                   | 16 |
| 2.2.4 Decorrelation Stretching Technique .....             | 16 |
| 2.3 Methods of Lineament Delineation .....                 | 17 |

|           |  |           |
|-----------|--|-----------|
| 2.3.1     | Manual Lineament Extraction.....   | 17        |
| 2.3.2     | Semi-Automatic Lineament Extraction .....                                    | 17        |
| 2.3.3     | Automatic Lineament Extraction .....   | 18        |
| <b>3.</b> | <b>LINEAMENT DELINEATION .....</b>   | <b>19</b> |
| 3.1       | Data (Imagery) .....   | 19        |
| 3.1.1     | Landsat-5 TM.....  | 20        |
| 3.1.2     | Advanced Spaceborne Thermal Emission and Reflection Radiometer (ASTER) ..... | 21        |
| 3.1.3     | Shuttle Radar Topography Mission (SRTM) .....                                | 23        |
| 3.1.4     | Stereographic Aerial Photographs .....                                       | 23        |
| 3.2       | Analyses .....   | 27        |
| 3.2.1     | Landsat-5 TM.....  | 28        |
| 3.2.2     | Advanced Spaceborne Thermal Emission and Reflection Radiometer (ASTER) ..... | 38        |
| 3.2.3     | Shuttle Radar Topography Mission (SRTM) .....                                | 47        |
| 3.2.4     | Stereographic Aerial Photographs .....                                       | 49        |
| 3.2.5     | Production of Final Lineament Map .....                                      | 51        |
| <b>4.</b> | <b>REMOTE SENSING MANIFESTATIONS OF THE SÜRGÜ FAULT ZONE ....</b>            | <b>56</b> |
| 4.1       | ASTER.....   | 56        |
| 4.2       | Stereographic Aerial Photographs.....  | 61        |
| <b>5.</b> | <b>GROUND TRUTHING: FIELD OBSERVATIONS AND PALAEOSTRESS STUDIES .....</b>    | <b>64</b> |
| 5.1       | Field Observations .....   | 64        |
| 5.2       | Palaeostress Studies .....   | 69        |
| <b>6.</b> | <b>DISCUSSIONS .....</b>   | <b>71</b> |
| 6.1.1     | Data .....   | 71        |
| 6.1.2     | Methods .....  | 73        |
| <b>7.</b> | <b>RESULTS AND DISCUSSIONS .....</b>   | <b>74</b> |

|                                 |    |
|---------------------------------|----|
| <b>8. RECOMMENDATIONS</b> ..... | 79 |
| <b>REFERENCES</b> .....         | 80 |
| <b>APPENDICES</b>               |    |
| APPENDIX A. ....                | 87 |
| APPENDIX B: GLOSSARY .....      | 89 |

## LIST OF TABLES

### TABLES

|           |   |    |
|-----------|---|----|
| Table 3.1 | Characteristics of the imagery used in this study* . . . . .  | 20 |
| Table 3.2 | The Landsat 5 TM images used in the analyses. . . . .   | 21 |
| Table 3.3 | The ASTER images used in the analyses. . . . .  | 23 |
| Table 3.4 | Specifications of the aerial photographs used in this study. . . . .  | 27 |
| Table 3.5 | Four gradient filters (modified from Süzen and Toprak, 1997) which were applied to Landsat TM images. . . . .   | 33 |
| Table 3.6 | Four gradient filters (modified from Süzen and Toprak, 1997) which were applied to Aster images . . . . .   | 43 |
| Table 3.7 | Number of lineaments extracted from SWIR bands of ASTER data. . . . .   | 45 |
| Table 3.8 | Parameters of LINE module that are applied to the band 9 of the ASTER data. . . . .   | 45 |
| Table 3.9 | Illumination azimuth angles used for producing shaded relief image from SRTM keeping sun elevation 30° and the direction of lineaments that will be enhanced. . . . . | 47 |
| Table 7.1 | Summary statistics of the lineaments obtained using various data sets and methods. . . . .  | 74 |
| Table 7.2 | Summary of the intermediate products and the final lineament map. . . . .   | 75 |

## LIST OF FIGURES

### FIGURES

|             |   |    |
|-------------|---|----|
| Figure 1.1  | Simplified tectonic map of Turkey showing major neotectonic structures and neotectonic provinces .....                                      | 2  |
| Figure 1.2  | Major tectonic structures in the vicinity of the Study area .....   | 4  |
| Figure 1.3  | Simplified geological map and active faults of the study area.....  | 5  |
| Figure 3.1  | Four Landsat TM frames covering the study area .....  | 22 |
| Figure 3.2  | Five Aster frames covering study area.....  | 24 |
| Figure 3.3  | Pseudo color coded subset of SRTM image.....  | 25 |
| Figure 3.4  | Flight lines of the aerial photographs overlaid on ASTER image..  | 26 |
| Figure 3.5  | Work flow followed during the study.....  | 27 |
| Figure 3.6  | Subset of mosaiced Landsat TM images covering SFZ.....  | 30 |
| Figure 3.7  | Lineaments extracted from Landsat TM mosaic using manual approach and corresponding length weighted bidirectional rose diagram.....         | 32 |
| Figure 3.8  | Lineaments extracted from Landsat TM mosaic using semi-automatic approach and corresponding length weighted bidirectional rose diagram..... | 35 |
| Figure 3.9  | Lineaments extracted from Landsat TM mosaic using full automatic approach and corresponding length weighted bidirectional rose diagram..... | 37 |
| Figure 3.10 | Subset of mosaiced ASTER images.....  | 39 |
| Figure 3.11 | Lineaments extracted from Aster mosaic using manual approach and corresponding length weighted bidirectional rose diagram....               | 41 |
| Figure 3.12 | Lineaments extracted from Aster mosaic using semi-automatic approach and corresponding length weighted bidirectional rose diagram.....      | 44 |
| Figure 3.13 | Lineaments extracted from Landsat TM mosaic using full automatic approach and corresponding length weighted bidirectional rose diagram..... | 46 |

|             |  |    |
|-------------|--|----|
| Figure 3.14 | Lineaments extracted from SRTM using artificial illumination with different angles and corresponding length weighted bidirectional rose diagram.....                                   | 48 |
| Figure 3.15 | Lineaments extracted from stereoscopic aerial photographs and corresponding length weighted bidirectional rose diagram.....  | 50 |
| Figure 3.16 | Process flow of the final lineament map for the study area.....  | 51 |
| Figure 3.17 | Resultant map obtained from overlying of the lineament map obtained from ASTER and Landsat TM using manual approach..  | 52 |
| Figure 3.18 | Resultant map obtained from overlying of the lineament map obtained from ASTER and Landsat TM using automatic approach .....   | 54 |
| Figure 3.19 | Final lineaments map obtained from overlying of the resultant maps of manual and automatic methods.....  | 55 |
| Figure 4.1  | ASTER image showing pressure ridges within an anastomosing en echelon pattern of faults .....  | 57 |
| Figure 4.2  | ASTER image showing dextrally displaced streams along the SFZ between Çelikhan and Sürgü.....  | 57 |
| Figure 4.3  | The displaced streams along the SFZ in around Derbent overlaid on ASTER image .....  | 58 |
| Figure 4.4  | Trace Master Strand of the SFZ near Sürgü Dam indicated with white arrows and overlaid on Decorrelation stretched ASTER image .....  | 59 |
| Figure 4.5  | A) Fault blocks developed in the southern side of the SFZ overlaid on the ASTER image. B) Domino style faulting proposed to explain the development of fault blocks along the SFZ..... | 60 |
| Figure 4.6  | Subset of an ASTER image depicting a very sharp trace of the SFZ .....   | 60 |
| Figure 4.7  | Aerial photo showing pressure ridges within an anastomosing en echelon pattern of faults (red) and dextrally displaced stream courses (blue).....                                      | 61 |
| Figure 4.8  | Deflected streams in E of Derbent and NW of Nurhak overlaid on the aerial photo .....  | 62 |
| Figure 4.9  | Aerial photo showing western part of the study area .....  | 62 |
| Figure 5.1  | General view of Kozaklı Basin and the pressure ridges in its northern margin PR .....  | 65 |

|              |  |    |
|--------------|--|----|
| Figure 5.2   | Abrupt elevation change and cataclasites developed along the westernmost end of the SFZ around Göksun .....                              | 65 |
| Figure 5.3   | Stratigraphical juxtaposition around Derbent .....   | 66 |
| Figure 5.4   | Slickensides developed in the western end of the SFZ around Göksun .....   | 67 |
| Figure 5.5   | E-W trending linear valley developed along the Kurucova Segment of the SFZ .....   | 67 |
| Figure 5.6   | Phacoids developed within a sinistral fault developed between the pressure ridges in the northern margin of the Kozaklı Basin .....      | 68 |
| Figure 5.7   | Shear zones developed within the SFZ around Site-3.....  | 68 |
| Figure 5.8   | Conjugate faults developed in Paleocene Volcanic units within the SFZ around Sürgü .....   | 69 |
| Figure 5.9   | Cyclographic traces of fault planes and constructed palaeostress configurations for each site .....                                      | 70 |
| Figure 7.1   | Simplified map showing the segments of the SFZ and orientation of horizontal components of constructed palaeostress configurations ..... | 77 |
| Appendix A.1 | Local lineament map of Sürgü Fault Zone .....  | 88 |

## ABBREVIATIONS

|                   |  |
|-------------------|--|
| ASTER.....        | Advanced Spaceborne Thermal Emission and Reflection Radiometer |
| DEM.....          | Digital Elevation Model  |
| DS.....           | Decorrelation Stretching                                       |
| DSFZ .....        | Dead Sea Fault Zone  |
| EAFZ .....        | East Anatolian Fault Zone                                      |
| Landsat MSS ..... | Landsat Multispectral Scanner                                  |
| Landsat TM.....   | Landsat Thematic Mapper  |
| NAFZ .....        | North Anatolian Fault Zone                                     |
| PC.....           | Principle Component  |
| PCA .....         | Principle Component Analysis                                   |
| PR.....           | Pressure Ridge   |
| SFZ.....          | Sürgü Fault Zone   |
| SRTM .....        | Shuttle Radar Topography Mission                               |
| UTM.....          | Universal Transverse Mercator                                  |
| WGS84 .....       | World Geodetic System 1984 Datum                               |

## CHAPTER 1

### INTRODUCTION

#### 1.1 Purpose and Scope

Turkey lies within the central sector of the Alp-Himalayan chain and it lies within one of the most rapidly deforming areas in the world. The active tectonic scheme of Turkey is dominated by transcurrent tectonics exerted by the dextral NAFZ and sinistral EAFZ along which the Anatolian Block is escaping westwards towards the Aegean Arc. Unequivocally, it is accepted that the beginning of transcurrent tectonics is resulted from the collision and further northwards convergence of the Arabian Plate along the Bitlis-Zagros Suture Zone in the since the Late Neogene. This also resulted in the escape tectonics due to lithospheric over-thickening of the Eastern Anatolia (Şengör *et al.*, 1985).

Currently, the eastern Anatolia is being deforming under compressional-extensional deformation dominated by strike-slip faults with considerable amount of reverse components (Dewey *et al.*, 1986). On the other hand, western Anatolia is dominated by extensional deformation dominated by normal faults with strike-slip components (Şengör *et al.*, 1985). These contrasting styles of deformation in the eastern and western end of Turkey are linked by domination of the strike-slip faults changing their character with compressional components to extensional components from east to west.

Although, most of the current research about active tectonic of Turkey is concentrated mainly on the NAFZ and the west Anatolian extensional Province (Şengör *et al.*, 1985), however, the number of studies in the EAFZ and its relationship with the DSFZ which is one of the most important structure along which the Arabian Plate is moving northwards in the Eastern Mediterranean area

is limited (Quennell, 1958; Perinçek *et al.*, 1987; Perinçek and Çemen, 1990; Yürür and Chorowicz, 1998; Rojay *et al.*, 2001).

The major structures near the junction of the EAFZ and the DSFZ are outlined in Figure 1.1. Among these, the SFZ is an enigmatic structure in having almost E-W trend which is transverse to most of the structures in the region and being dextral strike-slip fault with a reverse component within a sinistrally deforming zone. Yet, there is no study which addresses its kinematics geometry, deformation mechanism and kinematics, although, it has very crucial role in structural development and deformation style of the region in connection with the kinematics of the Arabian Plate.

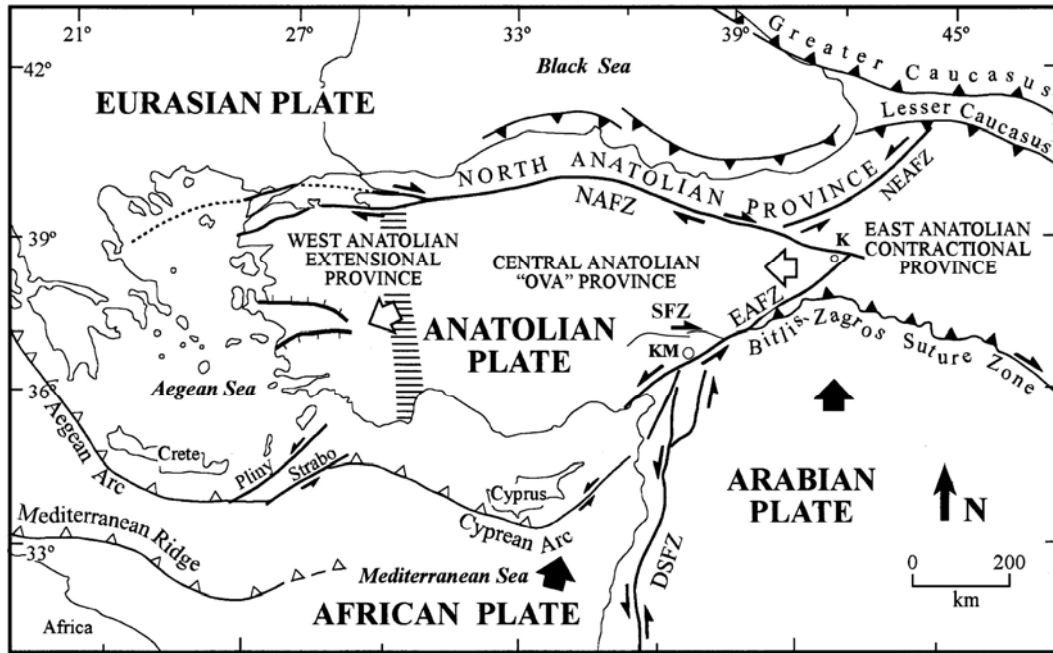


Figure 1.1 Simplified tectonic map of Turkey showing major neotectonic structures and neotectonic provinces (modified from Şengör *et al.*, 1985 and Bozkurt, 2001). K. Karlıova, KM. Kahramanmaraş, DSFZ. Dead Sea Fault Zone, EAFZ. East Anatolian Fault Zone, NAFZ. North Anatolian Fault Zone, NEAFZ. Northeast Anatolian Fault Zone, SFZ. Sürgü Fault Zone.

Therefore, the primary aim of this thesis is to introduce the geometry, deformation mechanism and kinematics of the SFZ using remote sensing (RS) techniques. The study includes delineating regional lineaments by using various image

processing and enhancement techniques. The recognized lineaments are used to extract structural outline of the region by detailed field studies that also involve fault slip analysis. In order to reach this goal, various data sources including Landsat-5 TM and ASTER imagery combined with DEM acquired from SRTM, and stereo-aerial photographs are extensively used.

## **1.2 Study Area**

The area under investigation located between Malatya–Adıyaman–Kahramanmaraş provinces in the east of Turkey (Figure 1.2) has an area of 16200 km<sup>2</sup> between 37° 30` to 38° 15` latitude North and 36° 15` to 38° 30` longitude East.

The study area and its vicinity are covered by the Sivas Sheet and Hatay Sheet of the 1/500 000 scale geologic map of Turkey prepared by Directorate of Mineral Research and Exploration (Ankara, Turkey). To perform this study, four Landsat TM images and four ASTER images are used. The information about these data is given in chapter 3.

The area that lies between the Malatya – Adıyaman – Kahramanmaraş (Figure 1.2) regions has a complex structure where different tectonic and geologic units of Turkey blended in a very complex array (Perinçek and Kozlu, 1984; Perinçek, 1987; Kozlu, 1987). For this reason, complexity of the region becomes a matter of research for several scientists. Several detailed and field oriented studies have discussed for understanding of this complex structure of the region (Perinçek and Kozlu, 1984; Perinçek *et al.*, 1987; Kozlu, 1987; Muehlberger, 1987; Şaroğlu, 1992; Yurtmen, 2002).

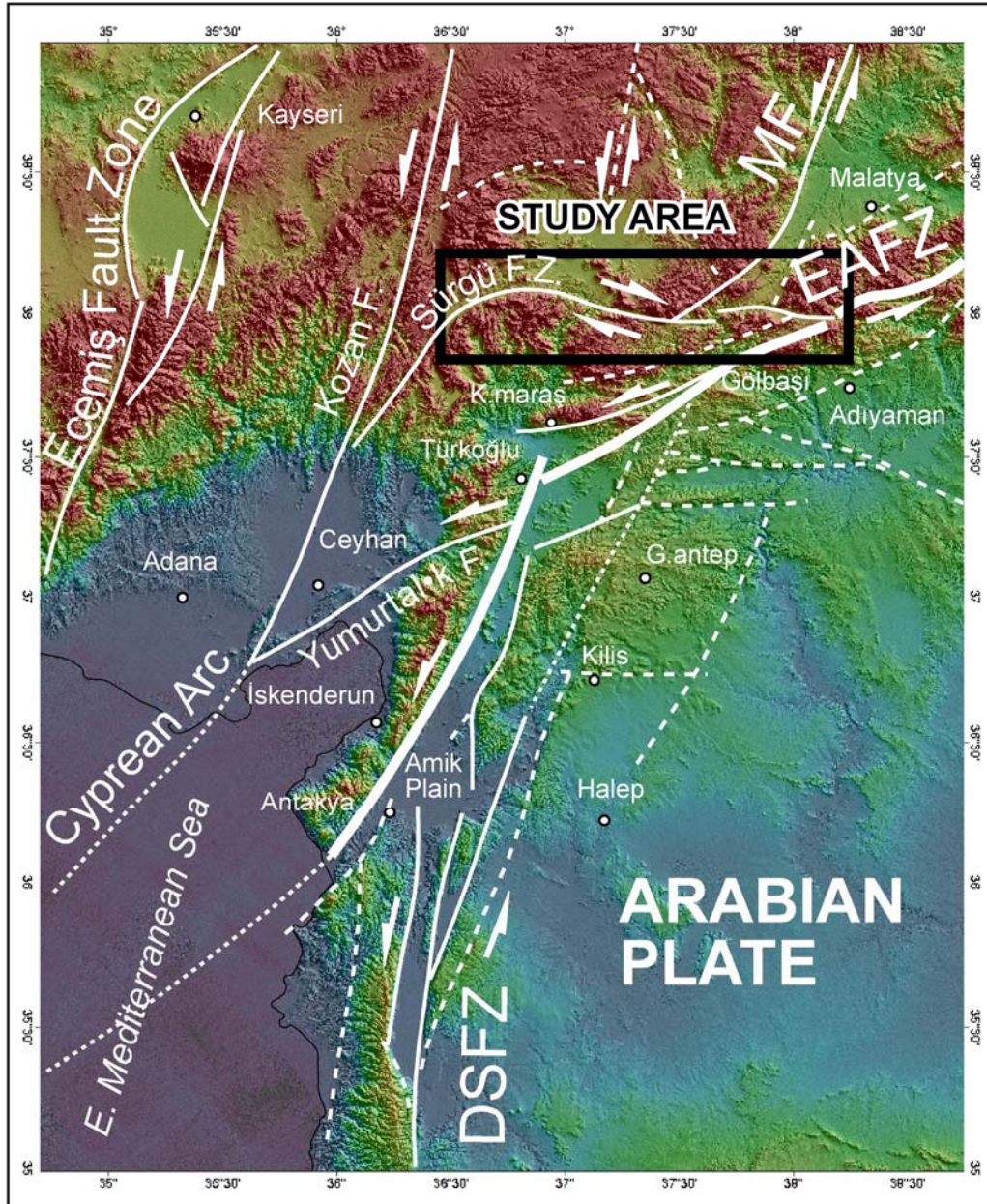


Figure 1.2 Major tectonic structures in the vicinity of the Study area (adopted from Rojay *et al.* 2001 and Kaymakçı *et al.*, 2005)

The main geological units exposed in the study area are outlined in Figure 1.3. this study is concentrated mainly on the structures including faults, lineaments and the folds, therefore any detail description of the tectonostratigraphy of the region is out of scope. We refer to Perinçek and Kozlu, (1984), Perinçek *et al.* (1987), Kozlu (1987), Muehlberger (1987), Yurtmen (2002), Kaymakçı *et al.*

(2005) for a comprehensive description of tectonostratigraphy and paleotectonic development of the region.

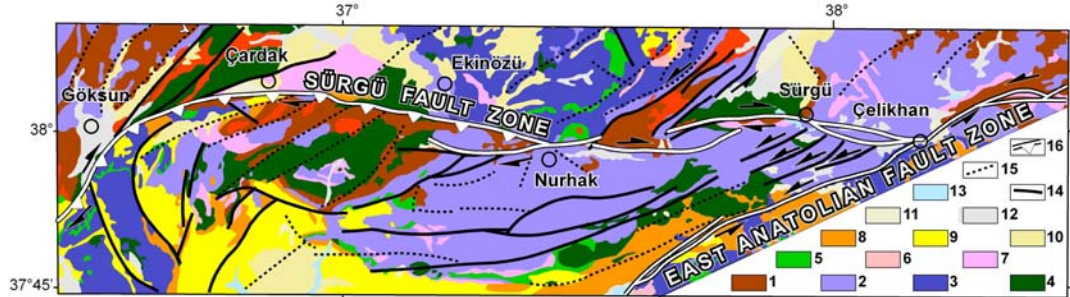


Figure 1.3 Simplified geological map and active faults of the study area (partly modified from 1/500.000 scale geological map of MTA). 1. Various metamorphic units, 2. Marbles, 3. Mesozoic Neritic Carbonates, 4. Ophiolite and ophiolitic mélanges, 5. Late Cretaceous units, 6. Late Cretaceous to Paleocene sedimentary and volcanic units, 7. Paleocene units, 8. Eocene units, 9. Neogene units, 10. Late Miocene to Pliocene units, 11. Late Pliocene to early Quaternary units, 12. Quaternary alluvials, 13. Water bodies (lakes, dams etc.), 14. Previously mapped active faults (major faults are indicated on the map), 15. Subordinate faults or faults with unknown activity, 16. Strike-slip faults with reverse component. Half arrows indicate direction of fault block movements.

### 1.3 Method and Context of the Study

This study integrates data sets obtained from various disciplines. Remote sensing, one of these disciplines, has been used extensively to provide information on geological lineaments that occur predominantly as faults and fractures. The remote sensing data, including satellite imagery, air photos and SRTM, constitute the most important data sets used in this study.

This study involves mapping of the active fault combined with processing and interpretation of satellite images, air photos and DEM obtained from the SRTM. The interpretations are based mainly on recognition of morphotectonic features such as lineaments and active fault traces, pressure ridges, sag ponds or local basins, alluvial fans, and river terrace, which are indicative of the active tectonics in the study area. Different enhancement techniques are applied to the images to get maximum information. Before the enhancement techniques are applied to the

images, it is imperative that for the best result, the dark pixel correction is used as the first step to remove haze. The enhanced image was draped over the digital elevation data to further improve the interpretations. Integration of DEM and image data displayed in 3D proves more effective for lineament extraction and lithological discrimination than 2D view approach. The active faults detected during the interpretation processes are digitized manually on-screen except for the automated lineament extraction method. After all the lineament data from different imagery are obtained, they are sorted out, depending on recognition of each lineament in each data set. Then, a final lineament map is obtained. Verification and accuracy assessment of the result map is performed by field studies during which fault slip data is also collected for kinematic analyses using palaeostress inversion techniques. On top of these main concern was given to the SFZ proper.

#### **1.4 Previous Studies**

Previous studies related to this study are classified into two groups. The first group includes the studies related to the remote sensing methods and the second groups include the studies related to the geology of the study area. These groups will be described in detail below.

##### **1.4.1 Studies Related to Remote Sensing**

Identification of lineaments is one of the applications of remote sensing in geology. There is no specific rule to extract lineaments on an image that are not readily observed on the ground. So, there are several studies addressed the problem of obtaining maximum information related to lineament detection and identification from the remotely sensed imagery. Most of these studies rely primarily on digital enhancement techniques together with the selection of optimum band(s) or band combinations that show “good” contrast.

The first remote sensing studies related to geological applications dates back to first aerial photo studies in the early 20<sup>th</sup> century. Aerial photographs were

successfully applied regional geological studies and mapping of active and de-activated (palaeotectonic) faults. After the Landsat images were publicized in 1972 a number of remote sensing centers were established all around the world and Landsat MSS images were used for delineating major structures and producing reconnaissance geological maps. In addition to these, a number of papers have been published about processing and application of Landsat imagery for various geological purposes. Some of the important papers that dealt mainly with usage of remotely sensed imagery for regional geological studies and lineament extraction techniques are summarized below.

Vanderbrug (1976) studied on three local line detection algorithms that could be applied to the satellite imagery. The experiments were conducted on detecting linear features in terrain on Landsat 1 images. Computer recognition (semi-automatic method) of the linear features which are of geological interest is the purpose of this study.

Qari (1991) tested the utility of the Landsat TM for lithological and structural studies. The scene was analyzed using various image processing techniques which include PCA, DS and edge enhancements for mapping different lithologies and structures.

Mah *et al.* (1995) aimed to delineate the lineaments by using color composite of Landsat TM bands 4, 5 and 7 which are edge-enhanced by asymmetric filters. In addition to Oari (1991), Mah *et al.* (1995) used different illumination direction to enhance the image for obtaining maximum information.

Akhir and Abdullah (1997) also studied on lineament extraction. The spatial filtering techniques were used to delineate the geologic lineaments.

Süzen and Toprak (1998) performed another study related with the lineament extraction. It was aimed to test different lineament extraction techniques including single band, multiband enhancements and spatial domain filtering techniques. Furthermore, a new algorithm which consists of a combination of large smoothing filters and gradient filters was developed to be able to determine regional lineaments.

Koike *et al.* (1998) proposed a method to calculate the azimuth of fracture planes through a combination of lineament maps and DEMs.

Arlegui and Soriano (1998) were suggested a methodology for selecting best band combination for visual interpretation Landsat-5 imagery for geological purposes and concluded that lineament identification is generally based on morphological rather than tonal contrasts. Lineament data was achieved using band-ratioing techniques and a lineament vector map produced using standard digitizing techniques.

Novak and Soulakellis (2000) also used Landsat-5 TM imagery combined with the fieldwork to detect lineament and geomorphic features. In this study, an algorithm was suggested for geological application of Landsat imagery which turned out to be one of standard procedures in geological remote sensing. These methods included use of PCA and False Color Composite (FCC). After image enhancement techniques were applied, the resultant lineament map was produced manually.

Madani (2001) studied on automatic lineament extraction. The utilization of the six bands of the Landsat TM bands was tested the and proposed the optimum bands for automatic lineament extraction. For this purpose, GeoAnalyst PCI EASI/PACE software is used with default parameters.

Ricchetti (2002) was one of the first who applied Landsat 7 (ETM+) imagery for regional geological studies. In this study a lineament analysis was carried out by combination of visual (manual) and semi-automated techniques including image enhancement techniques such as edge detection and morphologic filtering.

Similar study was performed by Leech (2003). This study was carried out in order to obtain best image for lineament analysis and identification, the geocorrected data were digitally enhanced using band ratioing techniques, linear and Gaussian nonlinear stretching, and PCA. A series of directional filters were applied to enhance the lineaments contained in the image. The resultant images were

visually assessed to determine the best combination for mapping significant lineament features.

In addition to Landsat TM data, the ASTER data is also used in this study. ASTER is a sensor that has high radiometric and spectral resolution that makes it particularly sensitive to small wavelength changes due to absorption of earth surface materials. ASTER also has a higher spatial resolution in the visible and near infrared ranges (first 3 bands is 15m) compared to Landsat (see Abrams *et al.* 2000 full account of the ASTER imagery). These factors make the ASTER sensor potentially more powerful for geologic applications especially lithologic mapping including the lineaments. The some important studies related with the ASTER data and lineament extraction are summarized below.

The first papers about regional geological application of ASTER imagery emerged after it become fully operational. Among numerous papers, Fu and Lin (2002) are worth to be mentioned here. They used ASTER image together with Landsat ETM+ imagery for detection of spatial distribution of surface rupture zone of an active fault. They applied contrast enhancement on various false color composites of combinations of ASTER and Landsat bands.

Another study performed by Rowan and Mars (2003) are related with the geologic mapping and discrimination of lithologic boundaries using ASTER imagery. Several important lithologic groups were mapped in their area of interest which have good exposure using spectral matching techniques. Ninomiya (2003) carried out similar study in which spectral indices were improved and lithologic mapping were performed. These studies are important for delineating the juxtaposed lithology that is indication of the probable fault trace.

Akman and Tüfekçi (2004) studied the faults and tectonic style of the part of Turkey based on remote sensing techniques. Landsat-TM and ASTER satellite data were used in visual interpretation. Several techniques based on DEMs that were extracted from ASTER data and produced by the contour maps were applied to interpret in the determination of the tectonic features.

Although there are numerous studies whose topics are related with lithologic discrimination using ASTER satellite data, there are a few studies related with the active fault mapping. The recent study of Fu *et al.* (2004) is one of those rare studies. In this study, Fu *et al.* (2004) were mentioned about the geomorphology and geometry of an active fault associated with an earthquake in southeast Iran. An active fault that ruptured during the earthquake was seen on three dimensional pre- and post-earthquake images generated from ASTER data. The remarkable geomorphologic features were detected by combination of the satellite imagery and field observation.

In order to extract the lineaments from remotely sensed data, an alternative approach is to use relief shaded images which were produced from DEMs of any resolution. Typical studies were conducted by Henderson *et al.* (1996), Cooper (2003), Jordan and Schott (2005).

Although a number of sophisticated semi- to fully automated techniques have been developed for lineament detection and extraction, visual interpretation is still the most reliable method for geological purposes because human perception can discriminate geological and non-geological lineaments (e.g. roads, crop-field boundaries etc) using contextual information. For this reason, in most of the studies, the manually extracted lineaments are assumed as a reference data to be able to evaluate the results of the semi automatic or automatic methods.

#### **1.4.2 Studies Related to Geology of the Region**

There is no study which is directly related to the SFZ. However, considerable attempts have been made to understand the nature, structure and geological evolution of this part of the SE Anatolia. These attempts can be divided into two basic categories such as 1) studies related to the tectonostratigraphical and structural evolution of the region and 2) studies related to the regional kinematics, including African, Arabian and Anatolian plates.

Perinçek and Özkaya (1981) is one of the first comprehensive studies which mapped and defined the geological units in the region. These units are

categorized as: 1) Metamorphic rocks: Bitlis, Pötürge, Keban and Malatya metamorphics 2) Complexes: Maden and Yüksekova, 3) Güleman Ophiolite 5) Autochthonous shelf deposits of the Arabian continent. In this study, it is tried to explain the development of the region based on observed field relationships.

Perinçek and Kozlu (1984) studied stratigraphy and structural relations of the units in the area that lies in the Adana–Kayseri–Malatya triangle. They classified the isopic zones and correlated them with the central and western Tauride isopic zones of Özgül (1976). They also categorized the ophiolites and ophiolite related units and mélanges and concluded that in the region some of the ophiolitic units were derived as allochthonous from the Northern Neotethys which formerly located between Pontides and the Taurides, in the Late Cretaceous. The other ophiolitic masses were derived from the southern Tethys formerly located between the Arabian Plate and Eurasian Plate, in the Late Miocene.

Yazgan (1984) demonstrates major tectonic units around Malatya and Elazığ and proposes a geodynamic model to clarify the evolution of Eastern Taurus belt. He discussed possibility of northwards double subduction and related ophiolite emplacement.

Kozlu (1987) proposed a model for the development of Kahramanmaraş basin and the development of some of the major faults in the region.

Perinçek *et al.* (1987) delineated all the major faults in eastern Turkey extending from the Ecemiş Fault Zone to Iran and Iraq. This study is one of the pioneering works in Turkey which attempted at delineating, mapping and describing the general characteristics of the major active faults in Turkey. Recent activity of the SFZ is discussed by this study for the first time. They claimed that the SFZ comprises a single through-going sinistral fault, rather than a fault zone.

The studies related to regional kinematics commonly aimed at determination of plate motion rates and directions in the region. Most of these studies proposed plate boundary conditions and fault blocks in order to determine strain fields in the region. Among these, Müehlberger (1987) is one of the first who studied the region suggested that the EAFZ is displaced by the SFZ.

Perinçek and Çemen (1990) studied a part the EAFZ using mainly satellite imagery and aerial photographs with limited ground control. They proposed that EAFZ is a sinistral transform fault between Arabian Plate and Anatolian block and meets the DSFZ around Gölbaşı Basin.

Similar study was carried out by Lyberis *et al.* (1992) who mapped out the EAFZ and proposed a plate motion configuration for the Africa – Arabia – Anatolia taking the Gölbaşı Basin as the triple junction. They extensively used the Landsat and Spot imagery also with limited field verification.

Karig and Kozlu (1990) proposed that Kahramanmaraş basin is a quadruple junction between EAFZ, DSFZ and Kahramanmaraş Fault.

Westaway (2004) proposed a new kinematic model and new motion vectors for the major plates and fault blocks in the region in order to update previously proposed models of Westaway (1994).

These studies are carried out in regional scale and none of them are directly related with the SFZ (SFZ) which is the main concern of this research. It has a key role in understanding its role in the evolution of the region since Neogene, regional kinematics and deformation mechanism of the region, as well as its current activity for its seismic potential.

## CHAPTER 2

### REMOTE SENSING AND LINEAMENT DELINIATION

In this chapter, brief theoretical information about the remote sensing, lineament and lineament delineation on the image is explained. Application of various image processing and interpretation techniques on detection and delineation of lineaments are also provided. The chapter comprises three main sections; 1) brief information about lineaments, 2) enhancement techniques that were applied in this study for lineament extraction, and 3) the methods used for extraction of the lineaments from the remotely sensed imagery.

#### 2.1 Definition of Lineament

Lineaments are of any linear features that can be detected as lines on remotely sensed images. The old term lineament, introduced at the beginning of the 20<sup>th</sup> century, was revised in the early seventies, as satellite images became more widely accessible (Karnkowski and Ozimkowski, 1999). O'Leary (1976) defined the lineament as a mappable, simple, or composite linear feature of a surface, whose parts are aligned in rectilinear or slightly curvilinear relationship and which differs distinctly from the patterns of adjacent features.

A lineament in satellite imagery and aerial photographs can be noticeable either darker pixels in the middle and lighter on both sides; or is lighter on one side and darker on the other side. Therefore, lineaments are identified by a series of adjacent pixels at the boundary of brightness changes on an image (Short, 2004).

Lineaments are originated from two types of sources. Firstly, lineaments may occur due to tectonic activity. This kind of lineaments usually corresponds to faults, joints and/or lithological boundaries. The other type of lineaments is due to man

made features including roads, railroads, crop field boundaries or any kinds of variations in land use patterns. First type of lineaments, occurred by the tectonic activity, is the main concern of this study.

## **2.2 Enhancement Techniques for Lineament Delineation**

Delineation of lineaments from the remotely sensed data is a complex process and includes uncertainties related to resolution and spectral characteristics of an image. Some of the uncertainties may be reduced using various image enhancement techniques which aim at improving the visual interpretability of an image by increasing the apparent distinction between the features in the scene (Lillesand and Keifer, 1999). Thus, digitally enhanced imagery helps to make optimal the complementary abilities of the human mind and the computer, i.e. the interpreter (human / computer) can extract more information.

Some enhancement techniques used for lineament extraction in this study are as follows;

- Contrast Enhancement,
- Color Composite,
- Principle Component Analyses (PCA),
- Decorrelation Stretching technique.

### **2.2.1 Contrast Enhancement**

Different objects reflect different amount of energy in a certain wavelength. This situation causes contrast between two adjacent objects. Depending on the amount of illumination, angle or incidence etc., same type of material may have varying amounts of reflection while different types of objects may reflect similar amount of energy. The variation in the amount of reflected energy determines the level of contrast. Contrast is also determined by the dynamic/radiometric range of a recording system. For most conventional remote sensing systems it ranges between 0-255 (8 bits). In many remotely sensed images, due to atmospheric and

other reasons the initial contrast range is much less than theoretical possible dynamic/radiometric range (min=1, max=1/255 or 255/1). The initial narrow range of digital values is expanded to utilize the full range of available digital values. So, the differences between features are emphasized. This can be done in various ways. The most widely used and the simplest ones include linear stretching, histogram equalization, piece-wise linear stretch, logarithmic, exponential stretching and normalization.

In each method the original values of an image are assigned to a new value to increase the contrast for whole or a specific range of the image. For full account of these methods we refer to Jensen (1996)

### **2.2.2 Color Composite**

A multispectral image consists of several bands of data. Each band of the image contains different amount of spectral information about the features on the surface according to wavelength (Jensen, 1996). For visual display, each band of the image is displayed using one band at a time, this produces a grey scale image. But, if combinations of three bands are used for visual display at a time, this produces a color composite image. If three original bands in red, green and blue (RGB) are chosen for visual representation, it is called true color composite. Color of the features are seen on the image what they are in real life. The other type is false color composites (Novak and Soulakellis, 1999). In this type of color composite, the colors of features look completely different from what they are in real life.

False color composites are used to highlight different features on Earth surface. Therefore, they are very useful for remote sensing studies. In color composites, in order to obtain maximum information and maximum contrast the bands with minimum correlation must be selected. For example, for more geological applications, the Landsat TM band combinations (RGB) 5, 3, 1 or 7, 3, 1 results best color contrast (Kaymakçı *et al.*, 2000).

### **2.2.3 Principle Component Analysis**

PCA is used to remove or reduce redundancy in multispectral data. That is, the bands of remotely sensed image often contain similar information. Through a transformation operation all the information contained within n-bands can be packed into fewer bands. In this way the number of bands to be processed is reduced and the computational efficiency is achieved without losing much information (Lillesand and Kiefer, 2000).

Spectral differences between features may be more apparent in PC images than in individual bands (Sabins, 1987). The Principal Component Analysis (PCA) is performed to obtain new channels in the lineament extraction process. So, these new components are used in color composites for getting more information about the lineaments (Novak and Soulakellis, 1999).

### **2.2.4 Decorrelation Stretching Technique**

DS technique is a modification Principal Component Analysis. As the name implies it is performed to decrease the correlation between two or more data sets using a transformation matrix.

DS is accomplished in four steps. In the first step, the covariance matrix is determined for the image and the eigenvectors are calculated. In the second step, the image is actually transformed from the radiance domain to PC space. It is just a special linear transformation of the radiance space, but the transformed data have the unique property that they are statistically decorrelated. In the third step, the PC images are separately contrast stretched. In the fourth step, the inverse transformation is calculated that would rotate the stretch data back to the original radiance space (Gillespie, 1992). The covariance of the enhanced images is reduced and least correlated part of the information is exaggerated.

DS is also carried out to obtain new informative components in the lineament extraction process. In order to obtain more information, these new components are used in color composites.

## **2.3 Methods of Lineament Delineation**

In lineament delineation from the remotely sensed data, there are some different methods developed by researchers (Wang and Howarth, 1990; Zlatopolsky, 1997; Süzen and Toprak, 1998; Ricchetti, 2002). The most widely used techniques are as follows;

- Manual Lineament Extraction,
- Semi-Automatic Lineament Extraction,
- Automatic Lineament Extraction,

### **2.3.1 Manual Lineament Extraction**

Lineament analysis is accomplished by visual interpretation after the enhancement techniques are applied to the image. The lineaments detected during the interpretation process are digitized directly on the image(s) on hard copies or on the screen.

The main advantage of the manual extraction is that it is easy to detect the non-geological lineaments such as roads, field boundary or fences with human perception (Kocal *et al.*, 2004). In other words, artificial or additive lineaments may occur when the other types of lineament extraction methods such as semi-automatic or automatic are used.

The main disadvantage of this method is that it is subjective and mostly not reproducible.

### **2.3.2 Semi-Automatic Lineament Extraction**

Various computer-aided methods for lineament extraction have been proposed (Koike *et al.*, 1995; Toprak and Süzen, 1998; Ricchetti, 2002; Jordan and Schott, 2004). According to these researches, semi-automatic methods are based on some digital image analyses techniques and visual interpretation. After the

enhancement techniques are applied to the image, the lineaments are identified using digital image analyses techniques such as filtering, edge detection, morphological operations or sun shading. And then detected lineaments are converted vector structure using software packages.

The main advantage of the semi-automated extraction techniques is that it guides the analyst to achieve the task in a faster way with respect to the manual method. On the contrary to this advantage, the resultant lineament map may introduce artifacts.

### **2.3.3 Automatic Lineament Extraction**

During the lineament extraction processes, the need for automation of lineament interpretation arises. This can be performed using computer assisted techniques. There have been significant approaches developed by researchers (Zlatopolsky, 1992; Wang and Howarth, 1990; Cross and Wadge, 1988) for automatic detection of the lineaments and curvilinear features from remotely sensed images. Algorithms contained by software packages are used for detecting lineament. The result lineament map is produced in vector structure.

The main advantage of the automatic extraction method is to reduce subjectivity and to help the analyst. In addition to that, the lineament map is performed in a faster way with respect to the manual and semi automatic extraction method. However, during this process, the linear features detected from the images do not always correspond to geological structures. Therefore, expert knowledge is always required to evaluate the extracted lineaments. The parameters used in automatic lineament extraction are described in the relevant section (Chapter 3).

## CHAPTER 3

### LINEAMENT DELINEATION

In this section, various lineament extraction techniques from remotely sensed imagery will be presented. For this purpose, Landsat TM, ASTER and SRTM images will be used in order to obtain regional lineaments that will be used for the analysis of tectonics of the region. Then, the study is concentrated on main course of the SFZ (SFZ) using aerial photographs. It is thought that the recognition of regional structures would improve understanding of development history and kinematics of the SFZ since its inception. However, before going into details of lineament analyses performed in this study, first brief information about the used imagery will be provided, then this section will continue with detailed description of lineament extraction techniques. At the end of each subsection extracted (resultant) regional lineaments will be presented.

This chapter comprises two main sections: the first section (Section 3.1) provides a general description of the data used for lineament extraction and the second section (Section 3.2) contains the performed analyses and the resultant maps of each data set.

#### **3.1 Data (Imagery)**

In this study, four types of remotely sensed data are used. These are as follows;

- Landsat 5 TM image
- Advanced Spaceborne Thermal Emission and Reflection Radiometer (ASTER) image
- SRTM image
- Stereographic Aerial Photographs

These data sets have different spatial and spectral resolution that control the constraints related to the size and geometry of the lineaments, and their precision and accuracy. Therefore, each of them has advantages and disadvantages related to the size and kinematic indicators to be detected. The detailed description of the used imagery is given in Table 3.1

Table 3.1 Characteristics of the imagery used in this study\*.

| Specifications  | LANDSAT TM   | ASTER   | SRTM   | AERIAL PHOTO                             |
|---|--|---|--|--|
| Available since   | 1975   | 2001  | 2003   |  |
| Spectral Res. (# bands)   | 7  | 14  | -  | Panchromatic or color photo              |
| Spatial resolution  | 30 m (6th band is 120m)  | Bands, 1-3 = 15m (including 3B), 4-9 = 30m, 10-14= 90m  | 1" & 3" (arc seconds)                              | Variable, few cm <                       |
| Ability to map  | Mineral groups, macroscopic structures                                   | Individual minerals, lithofacies, macroscopic structures  | Macroscopic structures but no spectral information | Mezoscopic structures, lithofacies       |
| Swath   | 185*185 km   | 60*60 km  | on demand  | on demand                                |
| Reliability/ precision of mapping   | Moderate (due to larger pixel size and mixed pixels)                     | Higher than Landsat   | 16 m vertical precision                            | The most reliable for structures         |
| Stereo  | no   | Yes, with off-nadir sensor working in NIR range (band 3B)   | Pseudo stereo can be produced                      | Yes, with 60% overlapping photos         |
| Advantages  | Easy to process, larger swath, blue wavelength, free, well calibrated    | Higher spectral resolution narrow band intervals, high ground resolution, higher dynamic range, stereo capability   | Elevation data, free                               | Stereo capability, ground resolution     |
| Disadvantages   | Less spectral resolution, less dynamic range (less sensitive), no stereo | More # bands to process smaller swath, no blue wavelength, still there are calibration problems, cheap but not free | No spectral information                            | Very low temporal resolution (~10 years) |
| *: only specific characteristics of the images related to this study are considered, other characteristics are ignored. Compiled from Lillesand and Keifer (1999) and Abrams (2000) |  |   |  |  |

### 3.1.1 Landsat-5 TM

TM image data consists of seven spectral bands. Six of them (1-5 and 7) cover visible infrared (VNIR & SWIR) bands with 30 meters ground resolution. The other is thermal band (band 6) whose spatial resolution during image acquisition is 120 meters (Table 3.1). For this study, the thermal band is not required.

Landsat-5 TM scenes were acquired with correction level 1 (L1G). That is, the scenes were radiometrically and geometrically corrected which were free from distortions related to sensor (e.g. jitter, view angle effect) satellite (e.g., attitude deviations from nominal), and Earth (e.g. rotation, curvature). However, the L1G product did not employ any correction based on ground control points or relief models to obtain absolute geodetic accuracy (Eurimage, 2005). Landsat-5 TM data acquired in WGS84 datum were resampled through nearest neighbor to convert into European Datum Mean 1950 (EDM50) into UTM Zone of 37.

For this study, four different Landsat-5 TM images were acquired on two dates: June 1989 and August 1989 (Table 3.2). All four images were cloud free and of good quality (Figure 3.1).

Table 3.2 The Landsat 5 TM images used in the analyses.

| Image No | Satellite Sensor | Path | Row | Acquisition Date |
|----------|------------------|------|-----|------------------|
| 1        | Landsat 5 TM     | 174  | 33  | 24.06.1989       |
| 2        | Landsat 5 TM     | 174  | 34  | 24.06.1989       |
| 3        | Landsat 5 TM     | 173  | 33  | 31.08.1990       |
| 4        | Landsat 5 TM     | 173  | 34  | 31.08.1990       |

### 3.1.2 Advanced Spaceborne Thermal Emission and Reflection Radiometer (ASTER)

ASTER image data consists of fourteen spectral bands. Three of them (1-3) are visible infrared (VNIR) bands with 15 meters ground resolution. The other six are short wave infrared (SWIR) bands with 30 meters ground resolutions. The others are thermal bands (band 6) whose spatial resolution is 90 meters (Table 3.1) (ASTER GDS, 2005). In addition, ASTER records the data in band 3B with a backward looking that enables the generation of DEMs as good as 15m ground resolution.

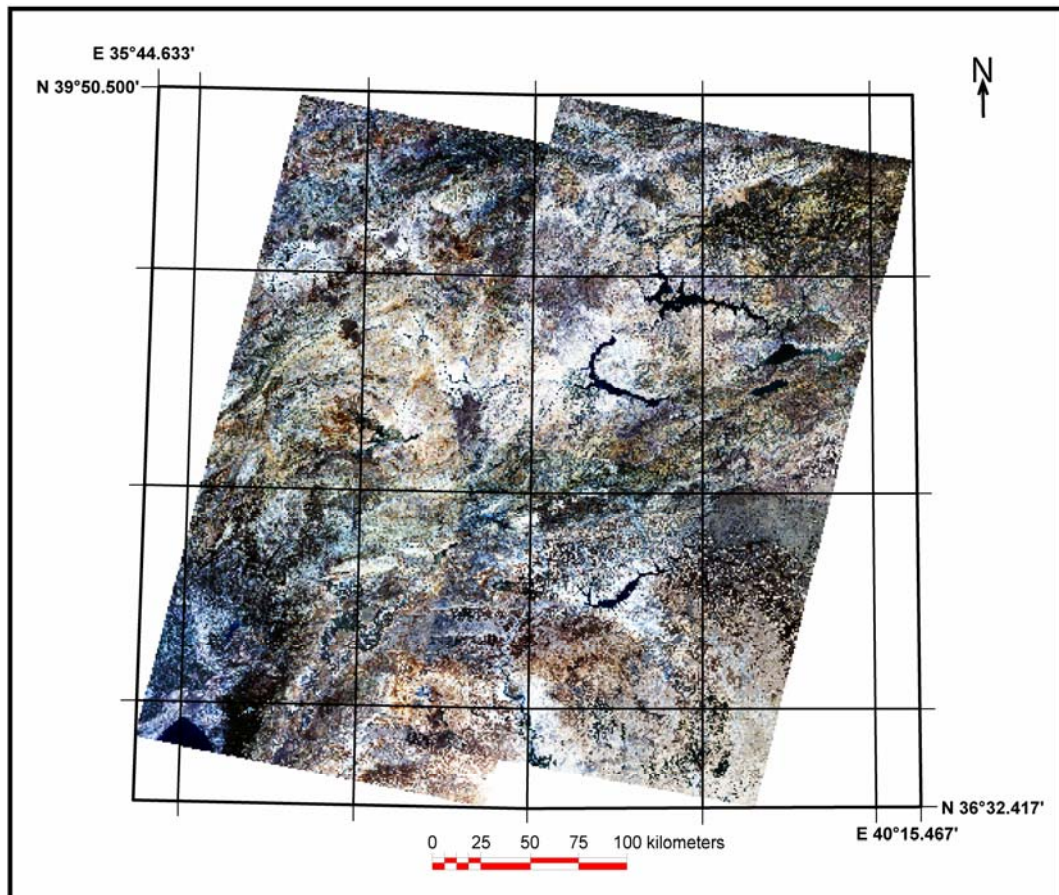


Figure 3.1 Four Landsat TM frames covering the study area.

ASTER scenes were acquired with system level 1B correction. This implies that the geometric and radiometric corrections were performed on Level 1A products. Therefore, distortions due to sensor, satellite and earth were removed from the image. In addition to that, band-to-band registration within and between the sensors were also performed. However, any correction based on ground control points was not applied to the ASTER Level 1B product (ASTER GDS, 2005). ASTER images were acquired in UTM projection system using WGS84.

For this study, five different ASTER images were acquired on two different dates: July 2001 and October 2003 (Table 3.3). All five images were cloud free and of good quality (Figure 3.2).

Table 3.3 The ASTER images used in the analyses.

| Image No | Satellite Sensor | Image Code                                | Acquisition Date |
|----------|------------------|---|------------------|
| 1        | ASTER            | AST_L1B_003_07112001083455_01182004154448 | 11.07.2001       |
| 2        | ASTER            | AST_L1B_003_07112001083446_01182004154650 | 11.07.2001       |
| 3        | ASTER            | AST_L1B_003_10052003082640_10192003093726 | 05.10.2003       |
| 4        | ASTER            | AST_L1B_003_10052003082632_10192003102346 | 05.10.2003       |
| 5        | ASTER            | AST_L1B_003_10212003082649_11032003100103 | 21.10.2003       |

### 3.1.3 Shuttle Radar Topography Mission (SRTM)

SRTM is developed to obtain elevation by radar interferometric data on a near-global scale. It consists of two radar systems called Shuttle Imaging Radar-C (SIR-C) and X-band Synthetic Aperture Radar (X-SAR). The SRTM data are provided at three resolutions. These are 1" (arc-second, ~30 m), 3" (arc-seconds, ~ 90 m) (NASA, 2005).

For this study, 3" SRTM data was obtained from USGS website as one of the available data source because of its spatial resolution, uniformity, and availability throughout the study area. Analyses carried out during this study were based on the use of 3" SRTM data acquired in geographic projection system with WGS84 Datum (Figure 3.3).

### 3.1.4 Stereographic Aerial Photographs

Aerial photography is one of the oldest and most versatile forms of remote sensing. It is a powerful tool for mapping earth features in their spatial context (Lillesand and Keifer, 1999).

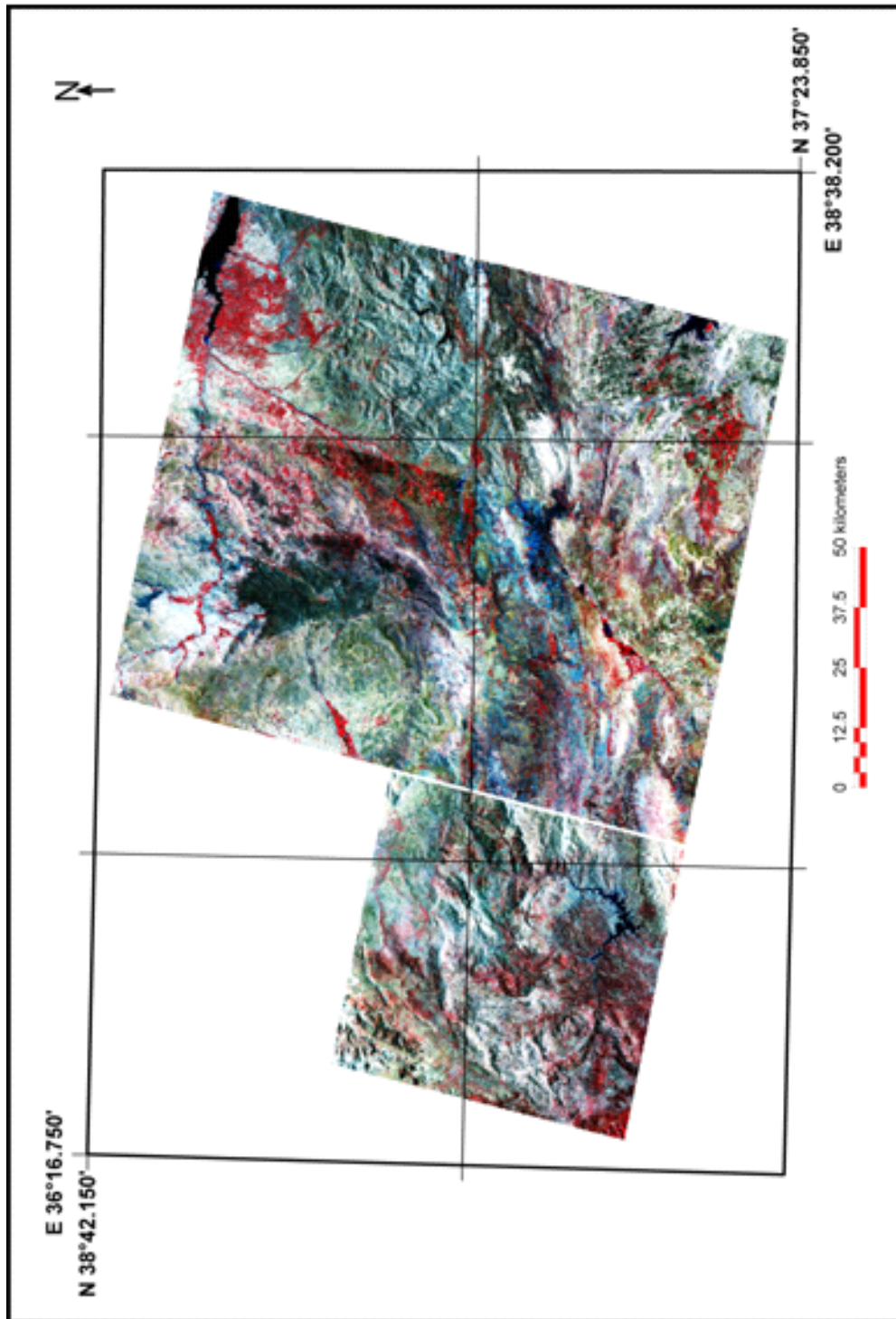


Figure 3.2 Five Aster frames covering study area.

Aerial photographs are generally taken in vertical direction (nadir) along flight lines. Vertical photographs are normally acquired in overlapping pattern, so in order to create a stereoscopic effect when adjacent pairs are viewed together. The overlapping views of the same ground area produce a parallax effect, which is also the basis for depth perception in human vision. This ability to perceive depth is quite useful for visual interpretation of air photographs (Lillesand and Keifer, 1999).

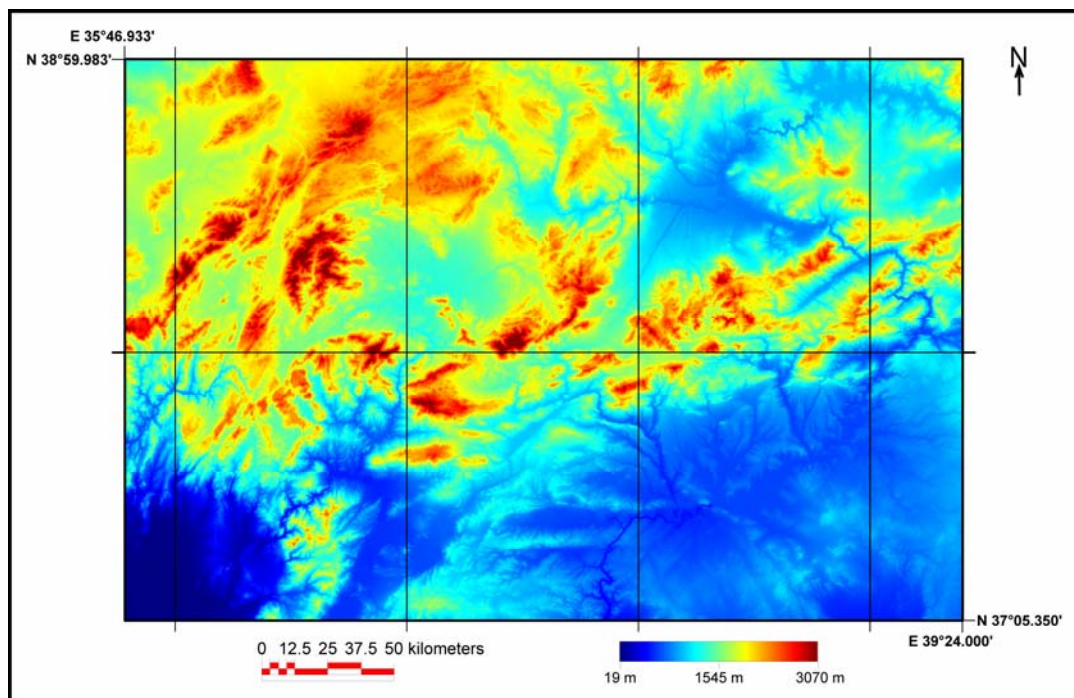


Figure 3.3 Pseudo color coded subset of SRTM image.

The basic elements are used to identify features on aerial photographs. These are tone, texture, pattern, shape, size, association and shadow. Among these, tone is the most elementary interpretive element. The other elements can not be useful to distinguish the features without tonal differences.

During this study, paper prints of stereo pairs of aerial photographs covering the area along the SFZ were acquired from the aerial photo archives at the General Command of Mapping (Ankara, Turkey). The flight index is given in Figure 3.4 and the characteristics of these photographs are given in Table 3.4.

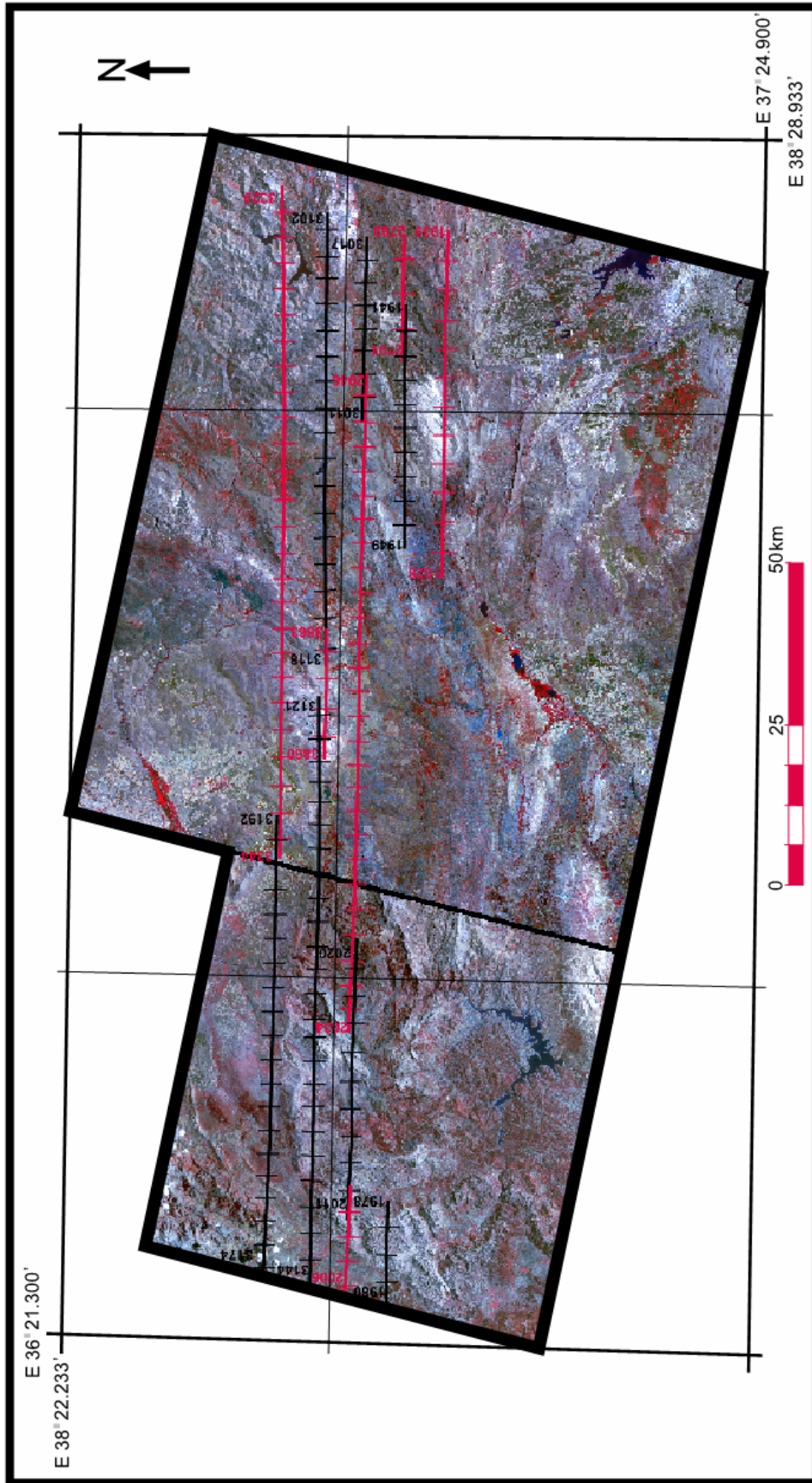


Figure 3.4 Flight lines of the aerial photographs overlaid on ASTER image. Each color corresponds to different set obtained in different flight campaign.

Table 3.4 Specifications of the aerial photographs used in this study.

| Aerial Photos |                           |
|---------------|---------------------------|
| <b>Color</b>  | Black and White           |
| <b>Date</b>   | Acquired in 1998 campaign |
| <b>Scale</b>  | 1:35.000                  |
| <b>Number</b> | 167                       |

### 3.2 Analyses

This section contains the analyses of the remotely sensed data in order to map out the regional lineaments in the study area. For each type of imagery different analyses techniques pertinent to that particular imagery are performed. So, this section is divided into four main parts. The work flow of the study is given in Figure 3.5.

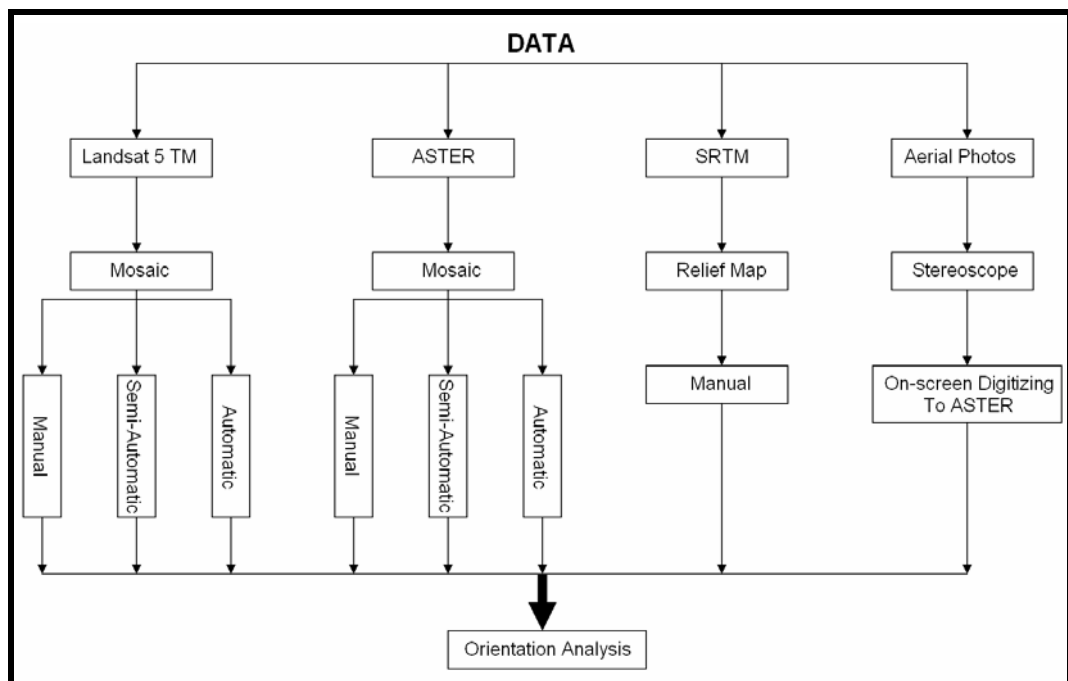


Figure 3.5 Work flow followed during the study

### 3.2.1 Landsat-5 TM

**Mosaicing of the Landsat Images:** The study area is located where four different scenes of Landsat-5 TM images are intersected. In order to produce a seamless single image of the study area, the four Landsat images were mosaiced.

Mosaicing of the Landsat-5 TM images is carried out by using ENVI 4.1 image processing software. During this process, four of the pre-georeferenced images are imported into the software package. The software contains algorithms that enable the user to perform mosaic operations relatively easily. But, some basic parameters have to be selected by the users such as resampling method, feathering, feathering distance, and color balancing. In order to obtain the most appropriate image, optimum values for parameters are selected. The resampling, one of these parameters, is carried out using the nearest neighborhood technique since it uses the nearest pixel without any interpolation and involves no change of the original pixel values. Another parameter is feathering technique. The edge feathering is selected to blend the overlapping areas on a specified blending distance. Finally, color balancing (histogram matching) is selected to be used for the entire image. For histogram matching, the histograms of all images were matched automatically by the software.

After the mosaic image is produced, the study area is extracted from the resultant image (Figure 3.6).

**Manual Lineament Delineation:** Manual lineament delineation is based on 1) selection of optimum band combinations to improve visualization of the image and 2) expert perception to understand geomorphologic signature on the image and to discriminate them into lineaments.

During this process, several band combinations are tested. Among of these, three of them found to be satisfactory. These RGB combinations are as follows; 5-3-1, 7-3-1, 7-4-2. In these combinations band 7 is sensitive to clay minerals, 5 is sensitive to iron-hydroxides and vegetation, 4 is sensitive to vegetation, 3 is sensitive to iron-oxides, 2 and 1 is sensitive to water beating minerals. Therefore,

each combination was used depending on the presence or absence of vegetation, red (iron bearing) soil and clay in the studied part of the images.

According to Canas and Barnett (1985) a standard color composite image (any three band display) contains 73% of the available image variance, whereas the principle composite image contains 97%. In order to involve all the bands in to a RGB display, a PCA is performed. By this way most of the information is compressed in to new channels. In this study, PC images are prepared using three visible (VIS) and three infrared bands of available sub-set of Landsat-5 TM mosaic. The first three PC images contain 98.33% of the information of the six Landsat-TM bands. Then, several combinations are tested again by using the new PC channels in combination with original channels. Finally, three different combinations are found to be satisfactory. First combination includes band 7 which is the most appropriate band for geologic investigations where clays are involved and other combinations include the first and the second PC channels respectively. The other two combinations include the band 3, PC1, PC2, and band 5, PC1, PC2 (RGB). During the lineament delineation process, all the combinations are spectrally enhanced using linear stretching of the histograms of the images.

In delineating the lineaments, the morphological signatures such as alluvial fans, sag ponds, displaced linear valleys and streams etc. that help to identify that the lineaments are taken into account and the final lineament map is produced (Figure 3.7).

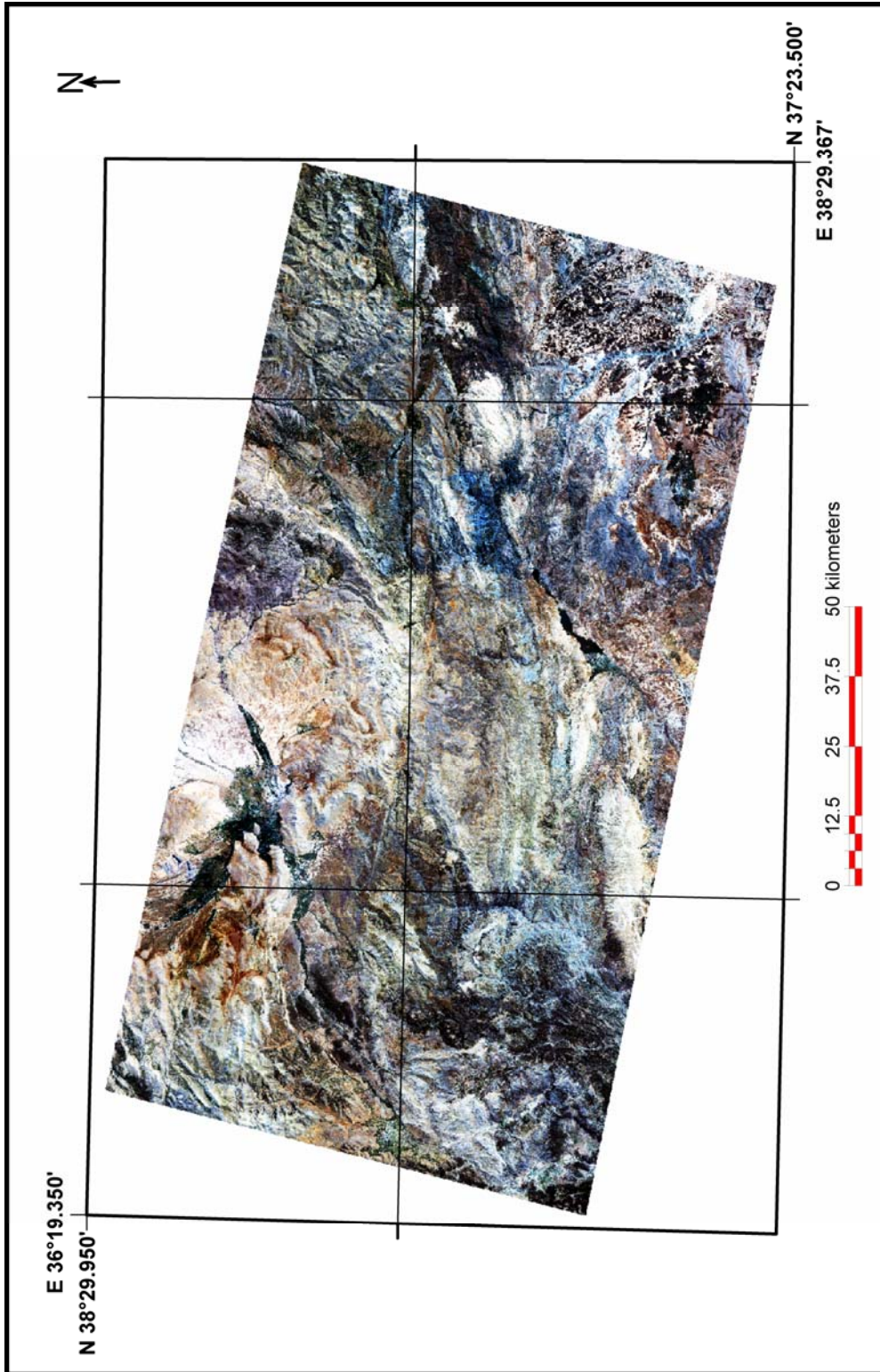


Figure 3.6 Subset of mosaiced Landsat TM images covering SFZ.

**Semi Automatic Lineament Delineation:** Semi automatic lineament delineation is based on 1) decision of the most appropriate band for edge enhancement filtering, 2) utilization of directional high pass filters that gives the best result to reduce subjectivity and to find lineaments that are not delineated by human eyes, and 3) on-screen manual digitization of recognized lineaments.

In order to perform selection of the band that gives the best result, six bands of TM are tested. The images of all six bands are compared in terms of contrast and definition of geological features. And then, it is decided to select band 7. In addition to this, it is least affected from the atmosphere in having relatively long wavelength that experience less scattering through the travel path in the atmosphere. Therefore, it shows good contrast and display geological lineaments compared to other bands (Süzen and Toprak, 1998; Madani, 2001).

After performing band selection, the second step is the selection of the filter type. For this purpose, two different types of filters are tested. Firstly, Sobel kernels are convolved over band 7 in four principle directions and filtered image added back to the original image. It is found that the outcoming result was not satisfactory.

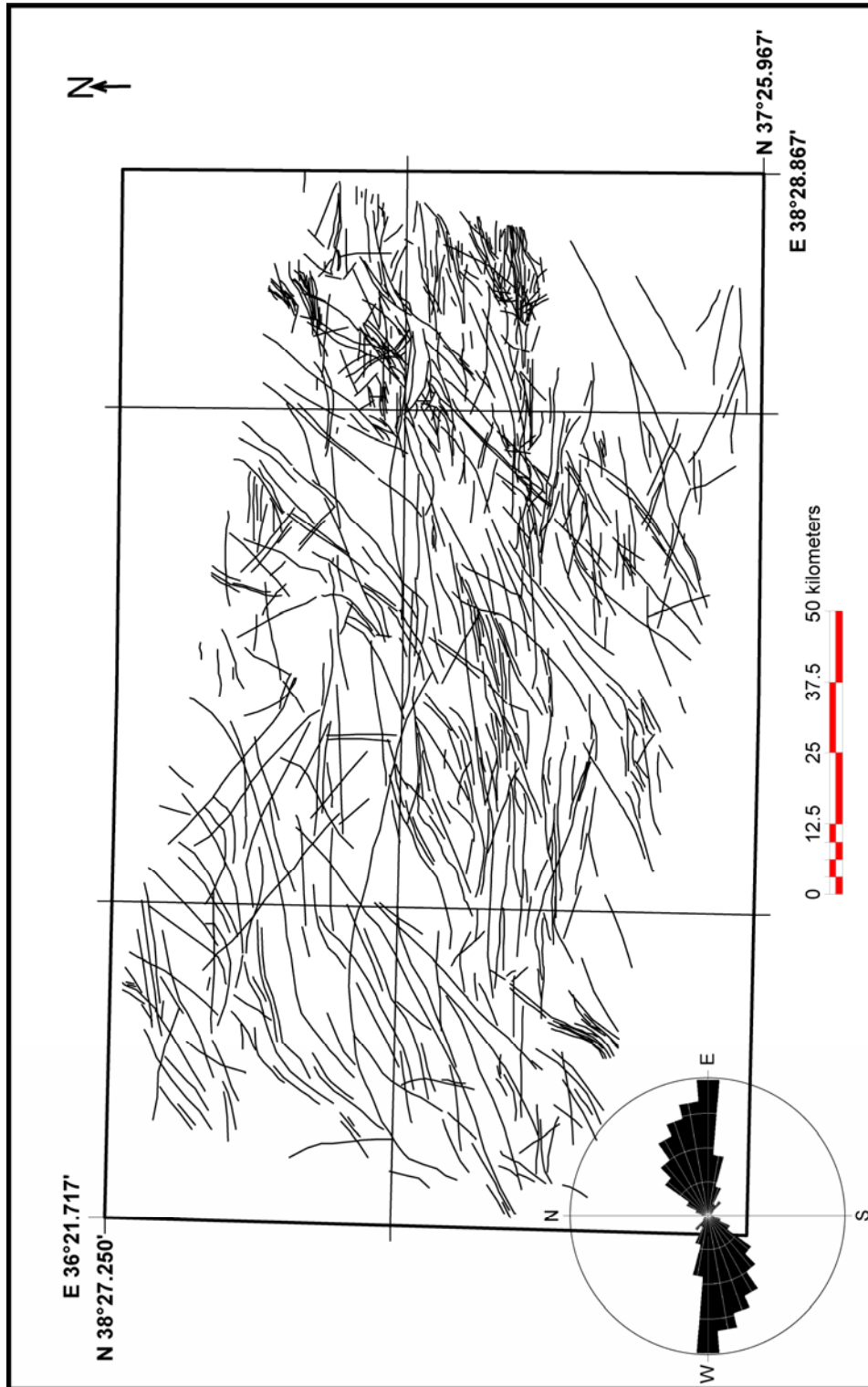


Figure 3.7 Lineaments extracted from Landsat TM mosaic using manual approach and corresponding length weighted bidirectional rose diagram. Note that E-W lineaments are dominated.



Four different filtered images are obtained after the gradient filters in four principle directions are applied. Then, the images are converted into binary images by applying threshold values. The most appropriate threshold value for each image is found to be 50. During threshold operation, values above 50 are assigned to 1; other values are assigned to 0. The binary images are multiplied by the original image (band 7); therefore the product images have original value of the band 7 where the pixel value is 1 on the binary images. After that, the product images are added back to the original image, to emphasize the edges. The final lineament map is produced from on-screen digitization of final image (Figure 3.8).

**Automatic Lineament Delineation:** Several commercial softwares are developed to deal with the automatic linear feature extraction from the images. In this study, automatic lineament extraction process is carried out with LINE module of PCI Geomatica v9.1.6 software. It automatically produces lineaments in vector format. The LINE algorithm consists of three steps: 1) edge detection, 2) thresholding and 3) linear/curve extraction into vector format. It works on single image channels. Therefore, steps mentioned above applied for each bands of the Landsat-5 TM image mosaics except for the thermal band (band 6). The visible bands have higher number of lineaments with respect to other bands. One of the reasons for this may be the effect of atmosphere which has higher influence on shorter wavelengths than the larger ones. Therefore, it is highly possible the artificial lineaments to occur in visible bands. In order to avoid this problem, band 7 is selected as input channel for the final results as was done in the semiautomatic lineament delineation section. This allows comparability of semiautomatic and automatic lineament delineation methods.

LINE algorithm is controlled by the following parameters: 1) RAD I, 2) GTHR, 3) LTHR, 4) FT HR, 5) ATHR and 6) DTHR.

RADI specifies the size of the kernel which is used as an edge detection filter during the operation. The large RADI value means less detail, larger (regional) lineaments and less noise. The kernel size is selected as 7 by 7 for this study.

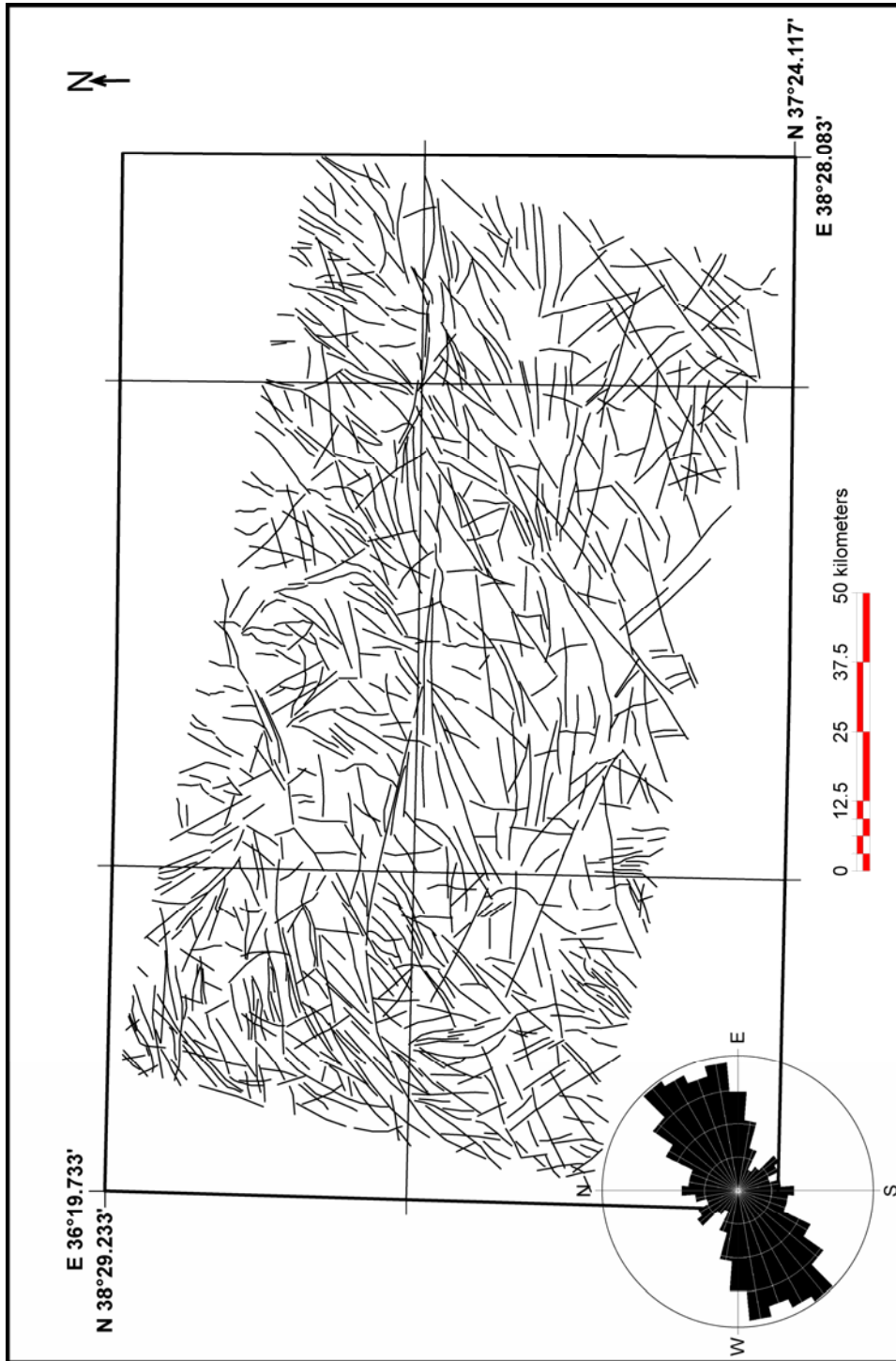


Figure 3.8 Lineaments extracted from Landsat TM mosaic using semi-automatic approach and corresponding length weighted bidirectional rose diagram. Note that NE-SW lineaments are dominated.

GTHR is the thresholding value for the minimum gradient level for an edge pixel. This value should be in the range 0 to 255 for 8 bit data. Different GTHR values are tested and 15 was found to be the optimum value. This value is selected according to its success of on delineating the visually evident fault trace on the image.

LTHR specifies the minimum length of curve to be considered as lineament. This parameter is selected as 50 that correspond to larger than 1500 m on the image. That means that the algorithm does not detect the lineament smaller than 1500 m.

FTHR is the tolerance allowed in fitting a polyline within a zone of pre-defined contrast zone (tunnel width) that will be assigned into lineament and specified in number of pixels. Lower FTHR values give better fitting but results shorter and larger number of segments. For this study, 2 pixels are selected for this parameter which found to be the optimum value.

ATHR means the maximum angle between two vectors for them to be linked. It is defined in degrees. 15 degrees are selected for this parameter.

DTHR specifies the maximum distance between the end points of two vectors for them to be linked. Different DTHR values are experimented and the optimum value is found as 100 pixels. This means that the algorithm links two vectors when the difference between them is less than 3000 m (PCI Geomatica Manual, 2001).

Before final parameter values are selected, several alternatives were tested to obtain the most representative lineament map. The final lineament map produced using LINE module of Geomatica is given in Figure 3.9.

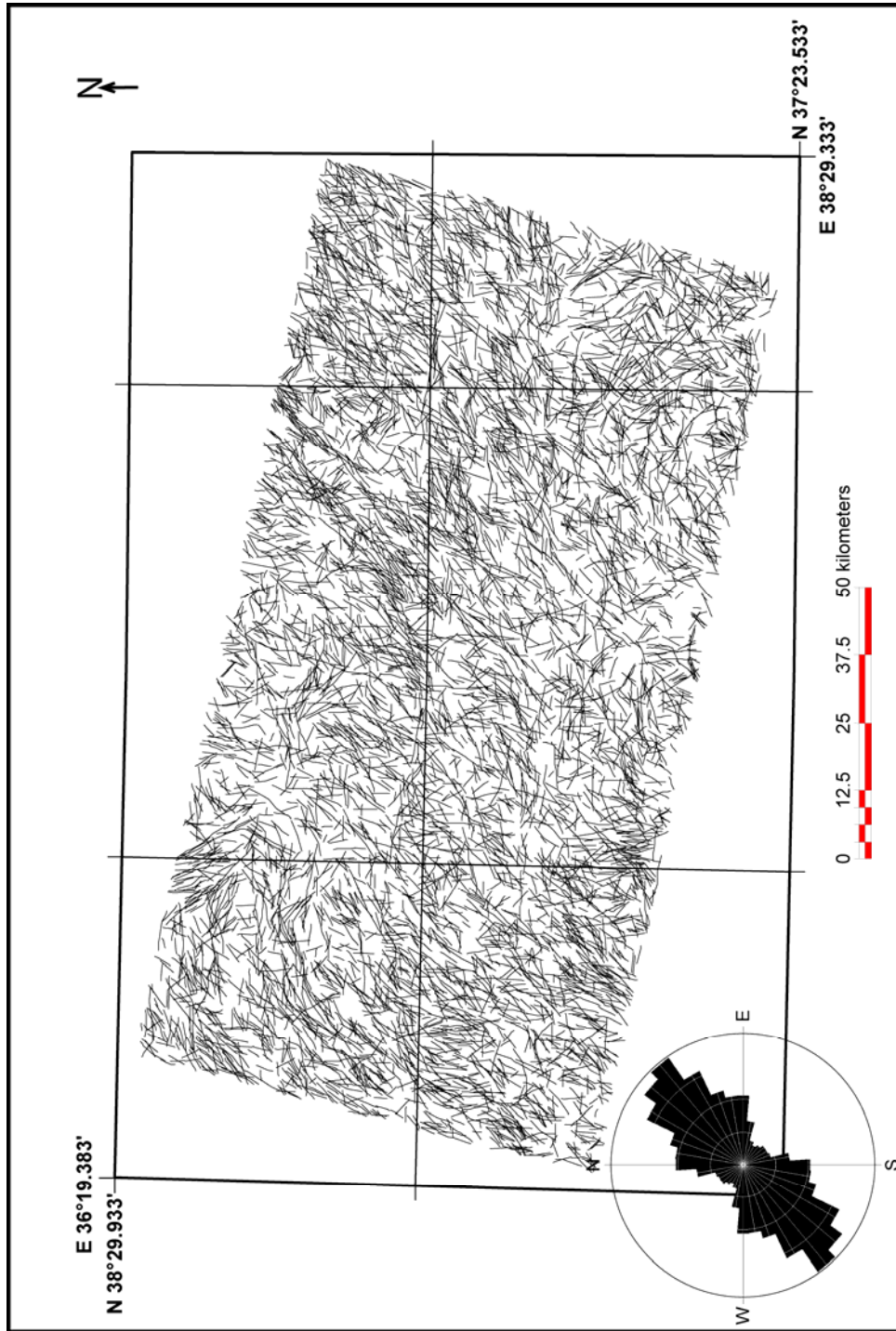


Figure 3.9 Lineaments extracted from Landsat TM mosaic using full automatic approach and corresponding length weighted bidirectional rose diagram. Note that NE-SW lineaments are dominated.

### **3.2.2 Advanced Spaceborne Thermal Emission and Reflection Radiometer (ASTER)**

**Mosaic of the ASTER Images:** The study area is covered by five different scenes of ASTER images. Because the swath width (60 x 60 km) of the ASTER scene is small with respect to the Landsat 5 TM; the area of interest is not represented within a single image. Therefore, in order to obtain consistent and coherent single image, these five different images must come together by using mosaic operation. For mosaic operations, three visible and near infrared (VNIR) and six infrared (SWIR) original bands of ASTER images are used. Before mosaicing process, SWIR (band 4-9) for each ASTER images are resampled into 15 m ground resolution by using nearest neighborhood technique.

TNT MIPS software is used for mosaicing. During this process, multiple georeferenced images are imported into the software package. Since the images were acquired in different time periods, in order to obtain best image display, the histogram of the 4th (Table 3.3) image which best resembles to Gaussian Curve (bell shape), is chosen as a reference histogram for the resultant mosaiced image. For warping the resultant image, the nearest neighbor technique is used in order to not alter the original pixel values. See Figure 3.10 for the resultant image.

Although, the most optimum mosaicing techniques and algorithms were used, following drawbacks were inevitable;

- There are missing parts between the images. This is due to incomplete image data, i.e. images are not overlapping (Figure 3.10).
- There is color contrast between the images. Because, images are acquired under different illumination and ground cover conditions due to seasonal variations.

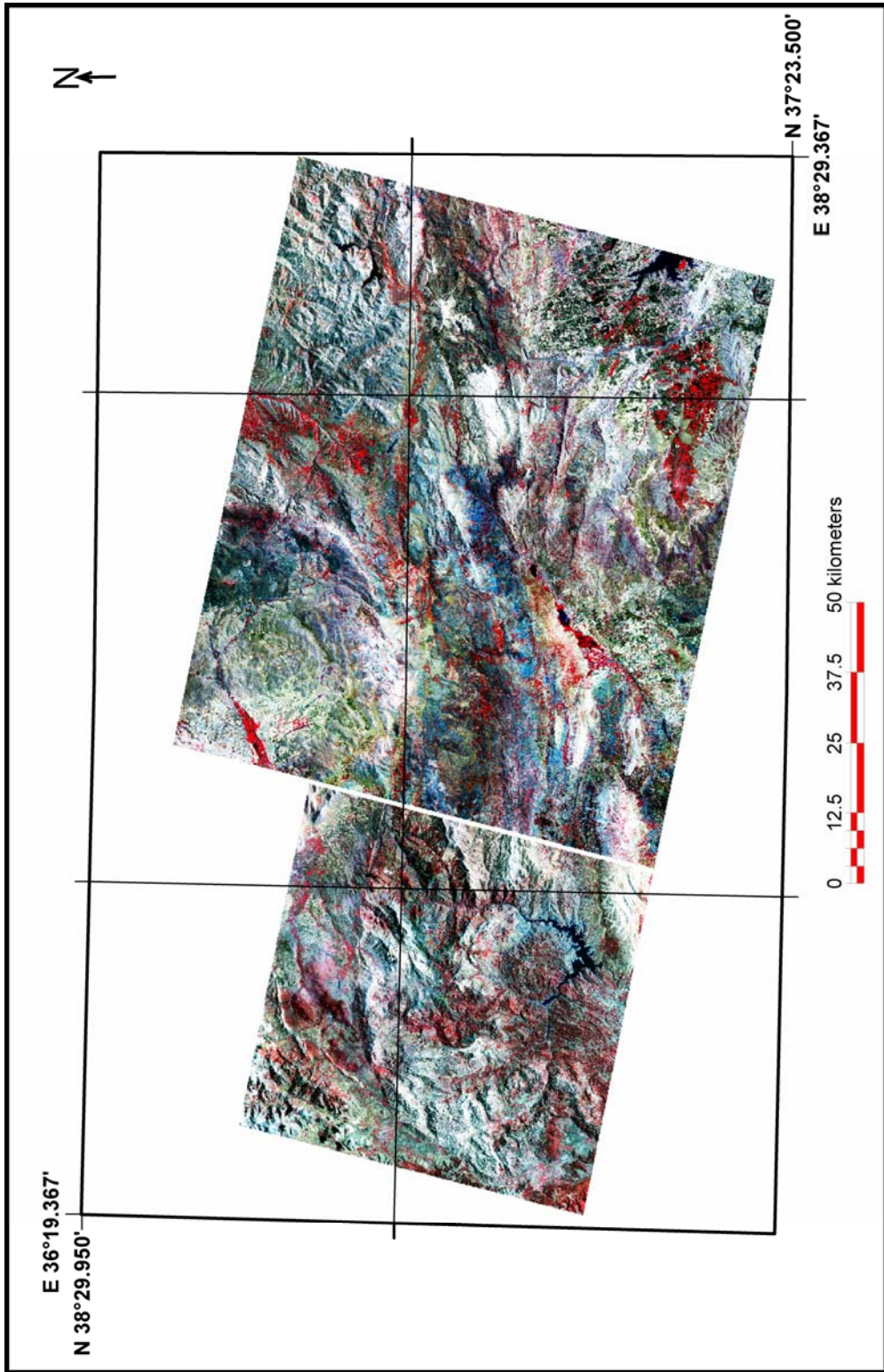


Figure 3.10 Subset of mosaiced ASTER images.

**Manual Lineament Delineation:** Delineation of lineaments manually from ASTER imagery is performed into two steps; 1) the selection of optimum band combination to obtain visually maximum possible color contrast, 2) on-screen digitization of recognized lineaments.

During this process, several band combinations are examined in order to enhance the images for discriminating the geologically meaningful linear features from the artifacts. Among various band combinations, the combination of bands 3, 2 and 1 in RGB display respectively found to be the combination having the best spatial resolution (15 m). In addition to this, RGB combination of 6, 3, and 1 found to be the best combination for color contrast. Besides, band combination 7, 3, and 1 (RGB) since most clay minerals are better detected in band 7.

In addition to RGB display of original bands, PCA is also performed to obtain new channels which have ability to compress 9 bands of the ASTER imagery into desired number of channels. Then, Principal Component (PC) images are produced from three visible and near infrared (VNIR) and six infrared (SWIR) bands of the subset of ASTER mosaic. The first two PC images contain around 97 % of the information. Therefore, first two components were indispensable. Several combinations that are formed using new PC channels are examined and two different combinations are found visually satisfactory. First combination includes the first three PC images which are formed PC3, PC2 and PC1 (RGB).

The other combinations consisting of PC1, PC2 and PC4 in RGB display respectively are also used during this process.

Ultimately, all the combinations mentioned above were also spectrally enhanced using linear stretching of the histograms of the images.

After selection procedures and linear stretching of the images, these combinations overlaid on to each other, and then the recognized lineaments were digitized manually directly on the screen (Figure 3.11). During this procedure, all the band combinations were used simultaneously. The lineaments that are recognizable in all combinations were selected as the final product, others were deleted out.

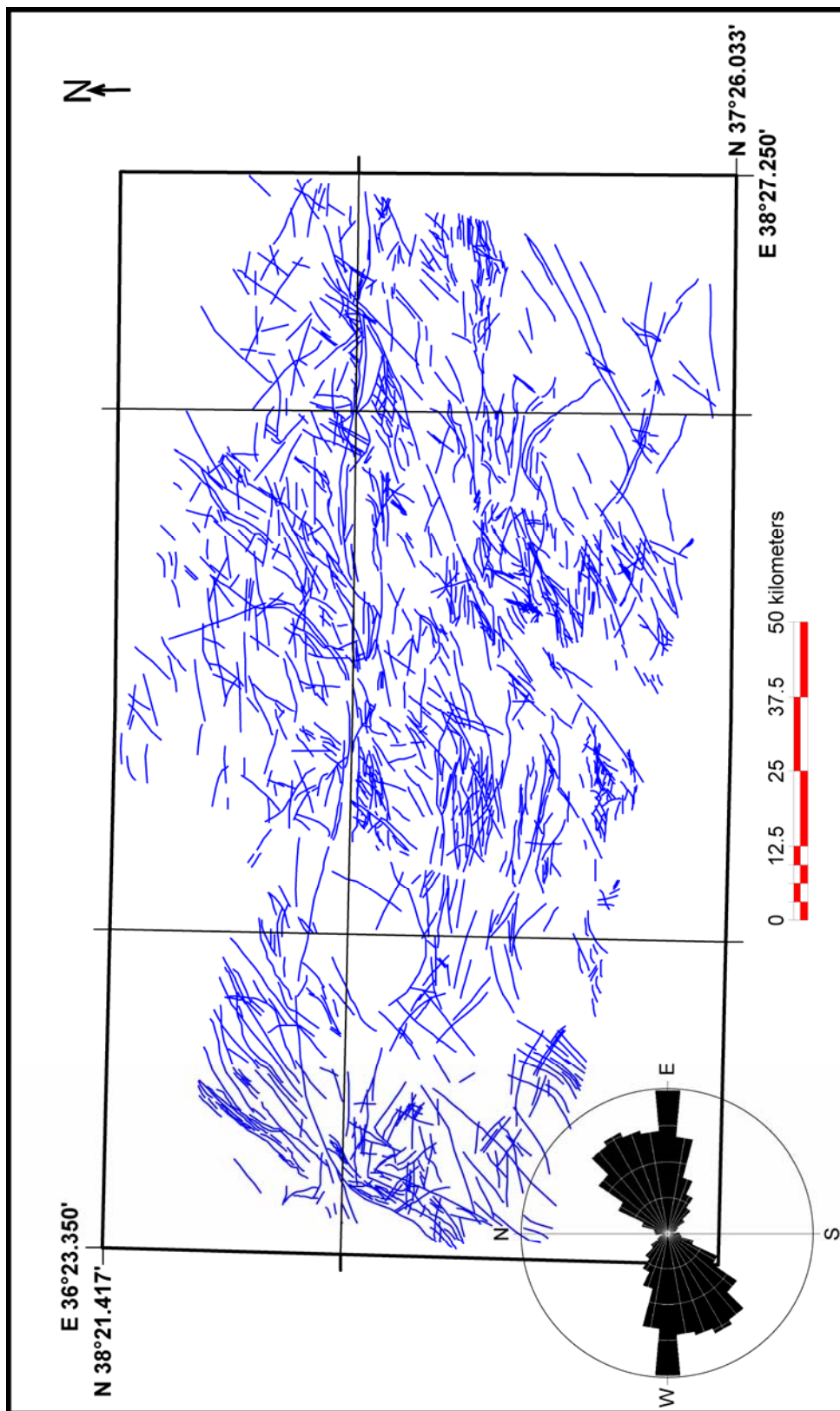


Figure 3.11 Lineaments extracted from Aster mosaic using manual approach and corresponding length weighted bidirectional rose diagram. Note that E-W lineaments are dominated.

**Semi Automatic Lineament Delineation:** Semi-automatic lineament delineation process is also applied to the ASTER data set. The same procedure outlined for Landsat-5 TM image is carried out to extract the lineaments from ASTER data.

The first step contains the selection of the appropriate band that can provide maximum information about lineaments. Nine bands of ASTER data are examined for this purpose. It is thought that the band 9 is the best choice due to having longer wavelength. Therefore, it gives good contrast and display geological lineaments compared to other bands because the contrast loss due to atmospheric haze is minimal.

The second step contains the decision of the filtering type that gives the best display of the lineaments. For this purpose, Sobel edge detection filters are convolved over the band 9, but the outcoming result is not satisfactory like Landsat TM data. This is because the 4-9th bands were resampled to 15 m. Then, the algorithm which consists of combination of large smoothing filters and gradient filters (Süzen and Toprak, 1997) are applied to the band 9 of the ASTER data. During the application of this algorithm, 12 by 12 smoothing filter is carried out over band 9. This process is used for combining small segments and reducing the noise of band 9. Finally, the 5 by 5 gradient filters which are modified from the Süzen and Toprak, (1997) are convolved over the smoothed image in four principle directions. Filters are applied during this process is given in Table 3.6.

After filtering process is completed, four different images containing edges located in different directions (N, S, NE-SW and NW-SE) are obtained. In order to eliminate the small segments on the filtered images, thresholding algorithm is carried out by testing different alternatives for each image. The threshold value for each image is found 15. As a result of the algorithm, the binary images are created. They are multiplied by the band 9 in order to obtain the original value of the band 9 where the pixel value is 1 on the binary images. After that, the product images are added back to the band 9 to emphasize the edges. The final lineament map is created by digitizing these edges on the four directional filtered images. The resultant lineament map produced using semi-automatic technique is shown in Figure 3.12.



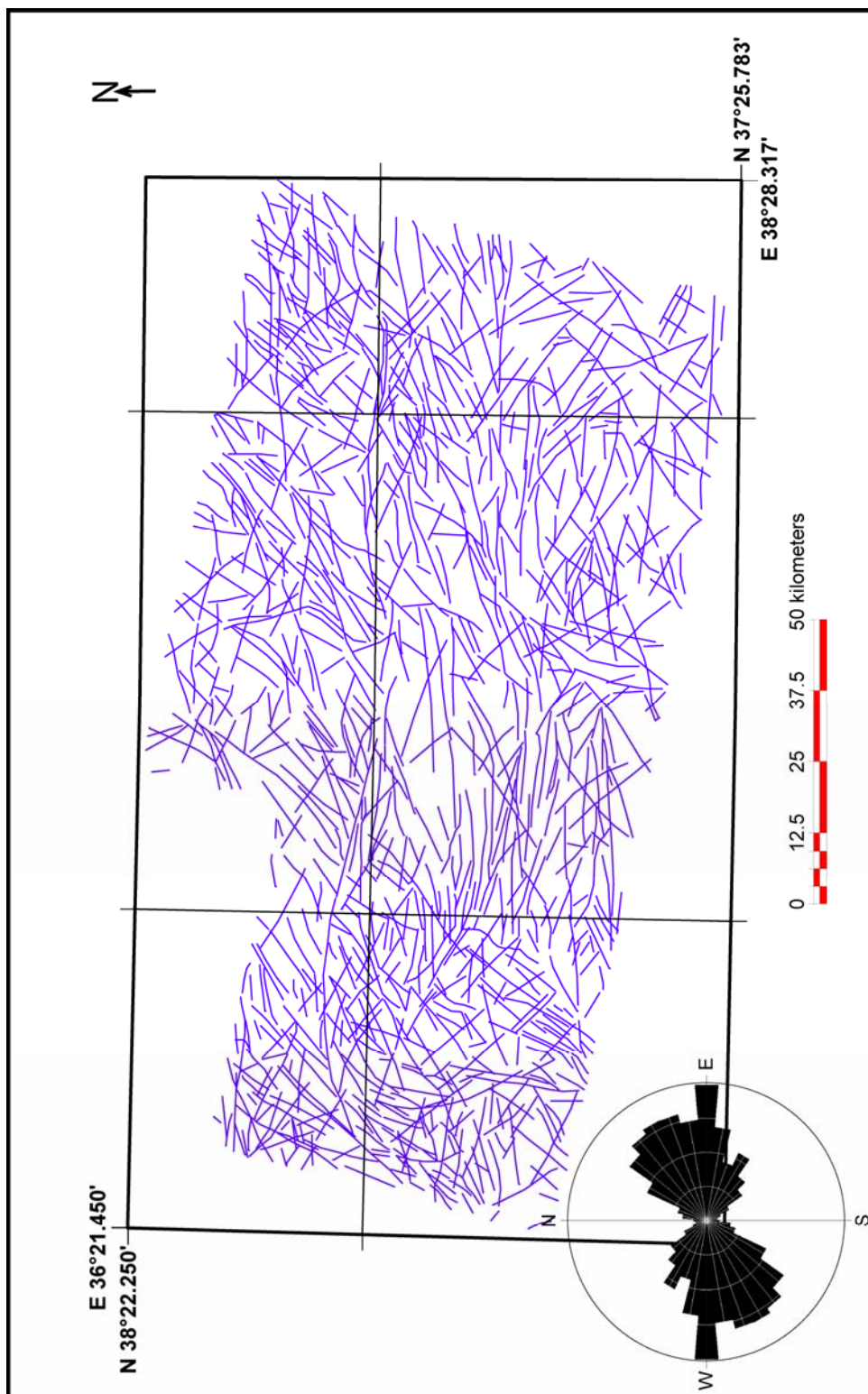


Figure 3.12 Lineaments extracted from Aster mosaic using semi-automatic approach and corresponding length weighted bidirectional rose diagram. Note that E-W lineaments are dominated and similar rose diagrams are obtained with the

It is found that the maximum number of lineaments are obtained in band 7 (see Table 3.7) and concluded that it is because of its sensitivity of various clay bearing units present in the region. Then the final lineament map of the study area (Figure 3.13) is produced in vector format by using parameters given in Table 3.8. However, the produced lineament map contains the linear features that do not correspond to geological features which are drainage lines, roads and farm field boundaries.

Table 3.7 Number of lineaments extracted from SWIR bands of ASTER data

| SWIR Bands | Number of Lineaments |
|------------|----------------------|
| Band 5     | 2848                 |
| Band 6     | 2840                 |
| Band 7     | 3467                 |
| Band 8     | 3170                 |
| Band 9     | 3435                 |

Table 3.8 Parameters of LINE module that are applied to the band 9 of the ASTER data

| Parameters of LINE Module | Parameter Value |
|---------------------------|-----------------|
| RADI                      | 11              |
| GTHR                      | 25              |
| LTHR                      | 90              |
| FTHR                      | 4               |
| ATHR                      | 15              |
| DTHR                      | 200             |

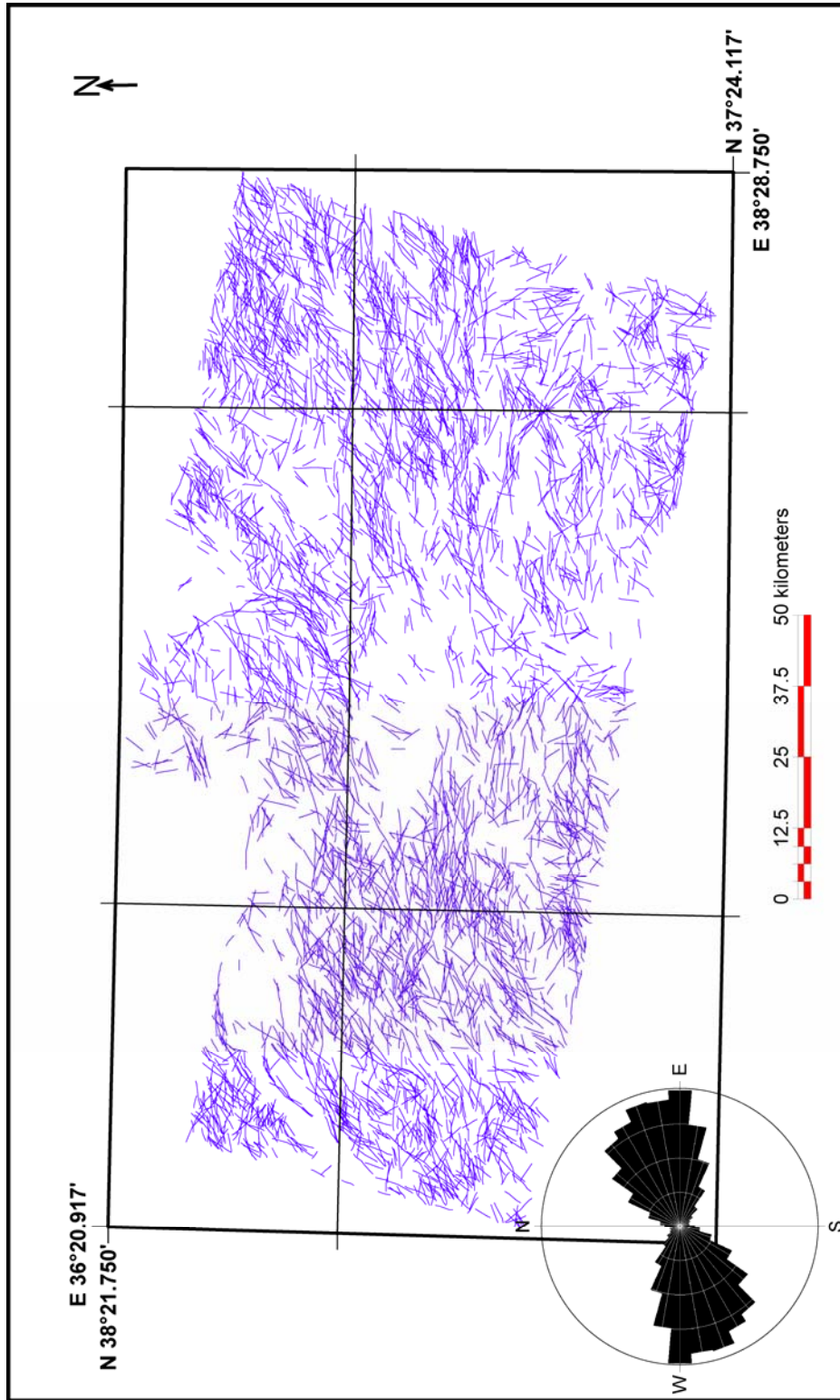


Figure 3.13 Lineaments extracted from Landsat TM mosaics using full automatic approach and corresponding length weighted bidirectional rose diagram. Note that E-W lineaments are dominated and similar rose diagrams are obtained with the manual and semiautomatic approaches.

### 3.2.3 Shuttle Radar Topography Mission (SRTM)

The present procedure contains the extraction of lineaments from shaded relief of DEM. This process is based on using artificial illumination sources in any angle. Therefore, DEM is illuminated synthetically to identify linear geologic structures. In order to perform this process, the SRTM data is used as elevation data. Shaded DEM data is produced according to two basic variables; 1) sun azimuth and 2) the sun elevation measured in angles from horizontal.

Linear geologic structures such as faults, fault zones and fracture systems lying at higher angles to the illumination azimuth are enhanced better than those lying at smaller angles (Cooper, 2003). In other words, if solar illumination directions follow east-west paths, linear features that have north-south trends are enhanced, while east-west trends are muted. Illumination azimuth angles that are used for delineation of the lineaments located in different directions are given in Table 3.9.

Table 3.9 Illumination azimuth angles used for producing shaded relief image from SRTM keeping sun elevation 30° and the direction of lineaments that will be enhanced. .

| <b>Azimuth of Light Source (Degree)</b> | <b>Direction of Lineament to be detected</b> |
|---|--|
| 0                                       | E-W  |
| 45                                      | NW-SE  |
| 90                                      | N-S  |
| 315                                     | NE-SW  |

The other variable is the elevation of the light source which affects the appearance of the lineaments. Choosing low angle for this parameter gives the best result since the low angle rays emphasize small differences in topography associated with linear features especially the depressions. For this study, elevation of the light source is selected as 300, after alternatives are tested. Then,

the lineaments are interpreted by displaying all the illumination combinations simultaneously. The resultant lineament map is depicted in Figure 3.14.

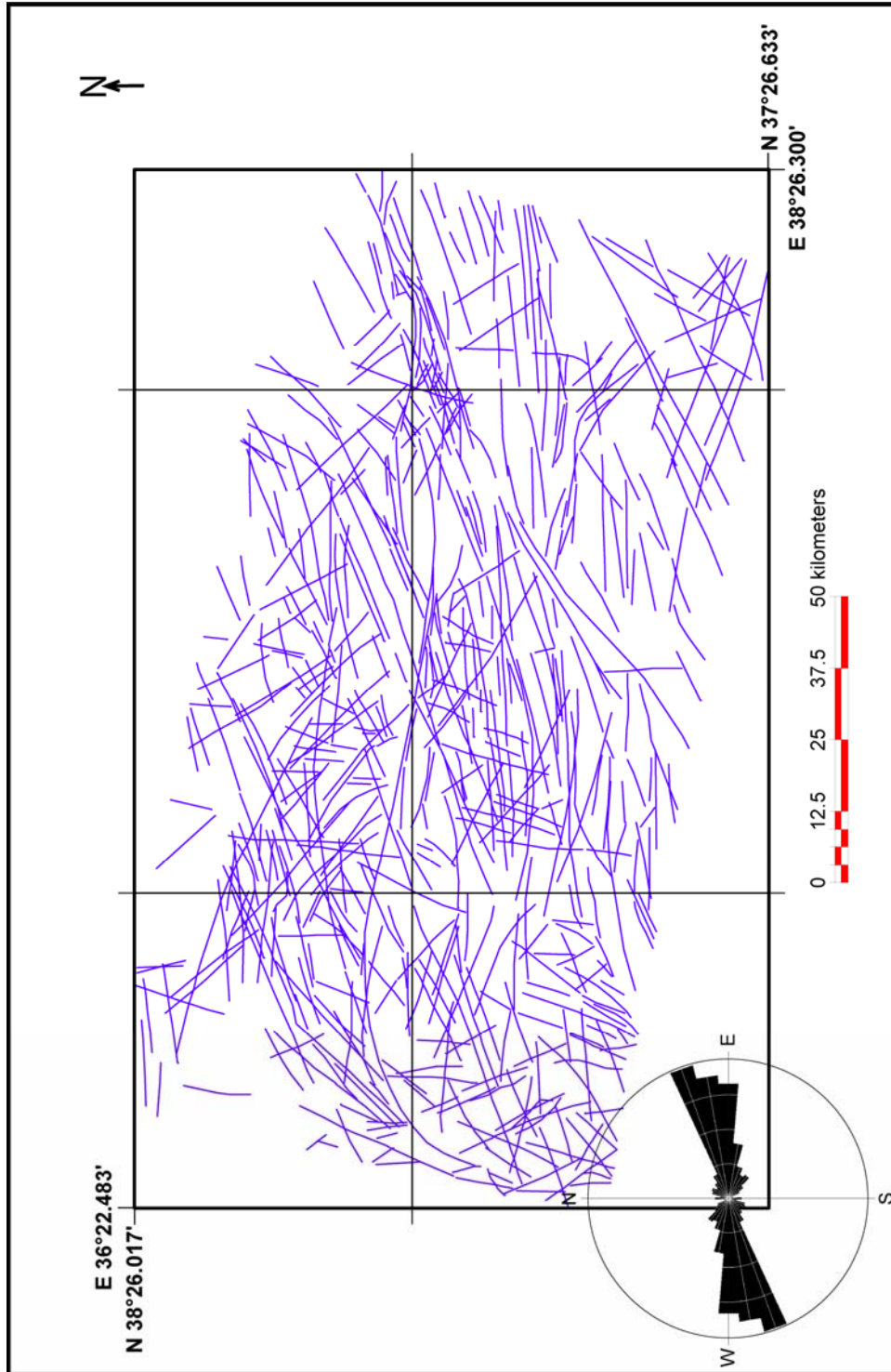


Figure 3.14 Lineaments extracted from SRTM using artificial illumination with different angles and corresponding length weighted bidirectional rose diagram. Note that ENE-WSW lineaments are dominated.

### **3.2.4 Stereographic Aerial Photographs**

The lineament maps produced from different kinds of remotely sensed data that have been mentioned in previous sections give the regional information about the study area. However, stereo pairs of aerial photographs are used for producing the local lineament map of the SFZ proper. The area is covered by the aerial photographs in three flight lines in E-W direction almost parallel to the SFZ.

During this study, 167 stereo pairs of aerial photographs are studied using mirror stereoscope. In delineating the lineaments, morphological features such as long linear ridges; alluvial fans and stream course deflections or truncations (contorting) disturbed stream network which are indication of active deformation are taken into consideration. All of these data are used to infer present activity and kinematic characteristics of the SFZ. Then the extracted lineaments are digitized on the ASTER imagery, which has comparable ground resolution, to avoid registration problems and the problems related to the nature of aerial photography. These include 1) platform induced distortions such as pitch, yaw, roll, drift and altitude change and 2) camera induced distortions such as radial displacement, relief effects etc. The resultant lineament map is depicted in Figure 3.15. After the digitization of the lineaments obtained from aerial photo study, an orientation analysis is carried out in the form of rose diagram (Figure 3.15).

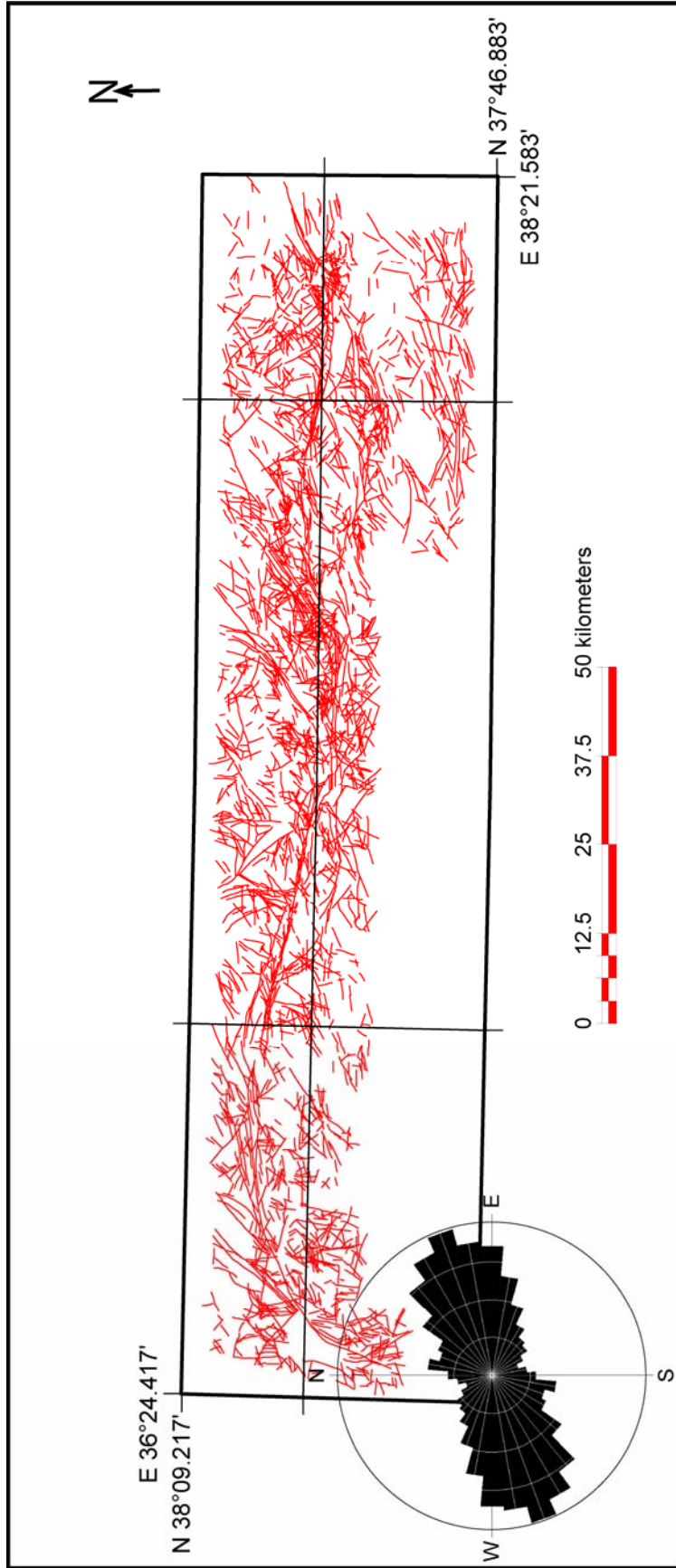


Figure 3.15 Lineaments extracted from stereoscopic aerial photographs and corresponding length weighted bidirectional rose diagram. Note that ENE-WSW lineaments are dominated and Malatya Fault trend (N10°-20°E directions) is also expressed. (see Appendix-A for a larger view of this figure)

### 3.2.5 Production of Final Lineament Map

This section contains the process that is carried out to produce a refined (final) lineament map of the study area. For this purpose, the resultant lineaments maps that are extracted from ASTER and Landsat 5 (TM) data using manual and automatic approaches are used to produce final lineament map. Lineament maps produced by semi automatic approach are not further analyzed since they are intermediate (hybrid) between manual and automatic approach.

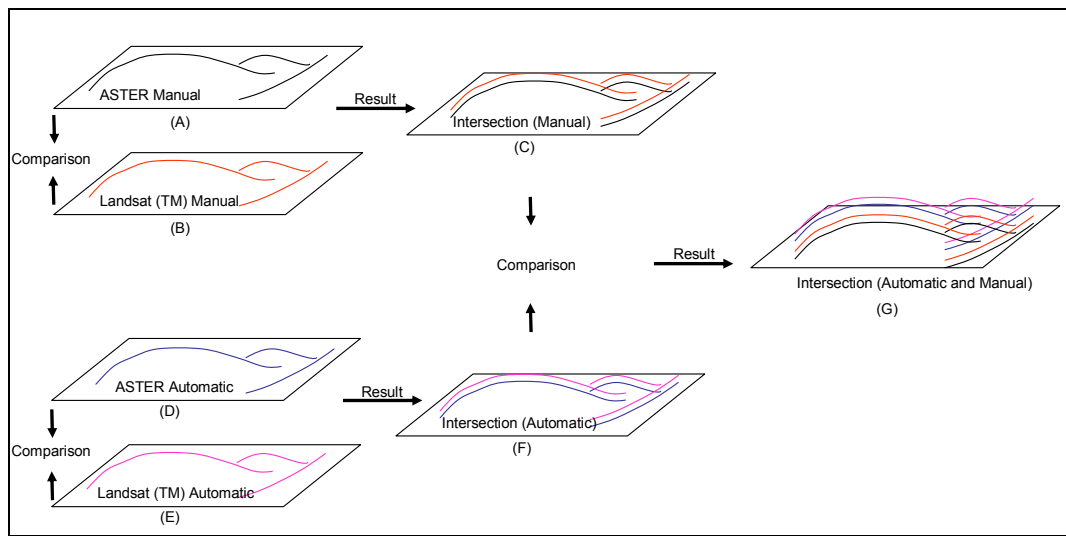


Figure 3.16 Process flow of the final lineament map for the study area.

Obtaining the final map consists of three steps. The first step contains the overlaying of the manually extracted lineaments from the ASTER and Landsat TM imagery (Figure 3.16 A & B). The lineaments that are common in both lineament maps are sorted out (Figure 3.16 C) in which the total lengths of the lineaments is 5938825 m. The ratio of overlapping lineaments (Figure 3.16 C and 3.17) compared to the total lineaments of the lineaments extracted from ASTER imagery (Figure 3.16 A) is 77% while it is 83% for the Landsat TM imagery (Figure 3.16 B).

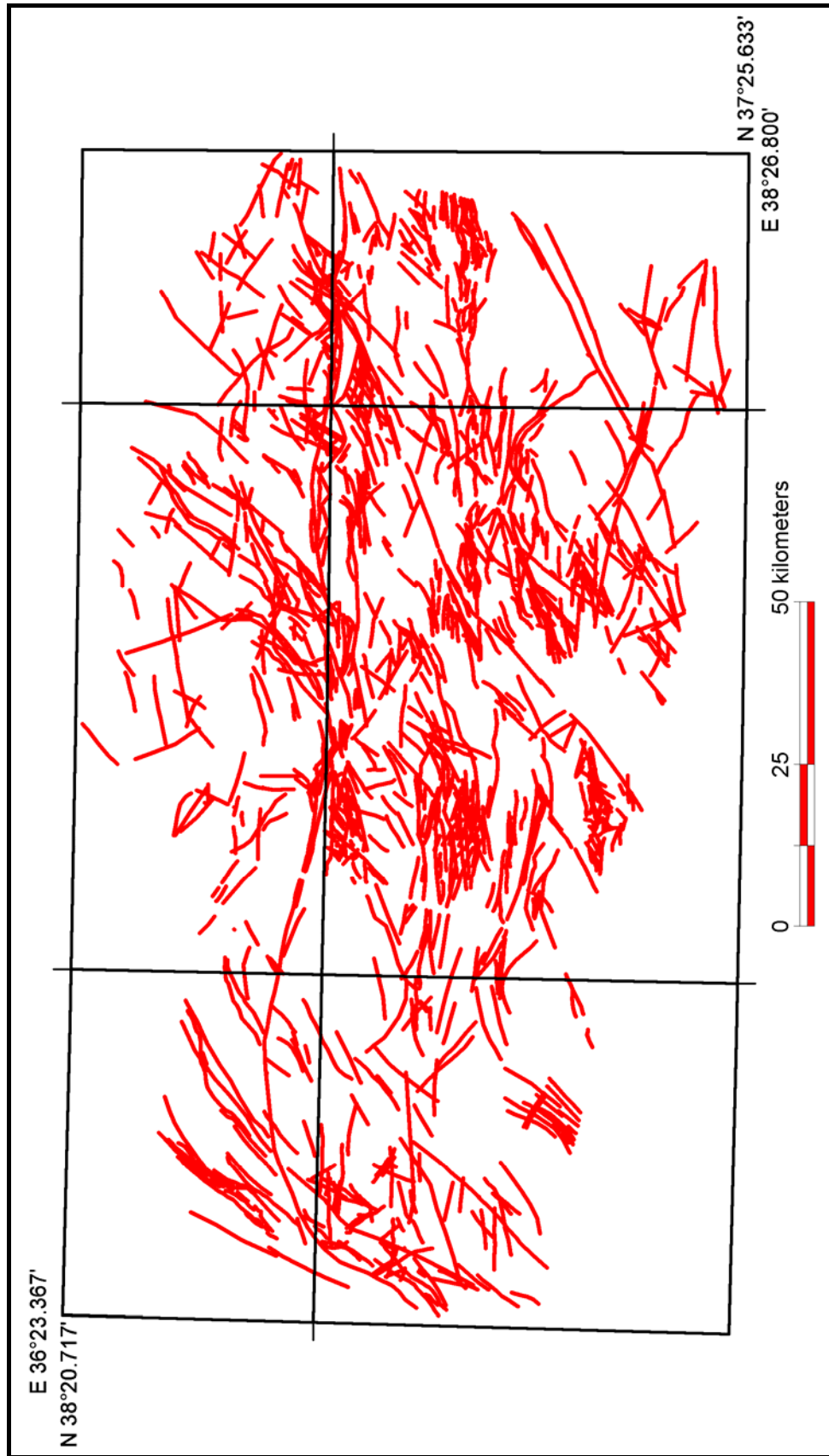


Figure 3.17 Resultant map obtained from overlaying of the lineament map obtained from ASTER and Landsat TM using manual approach.

The second step includes application of the same procedure for overlapping and comparison of the lineaments (Figure 3.16 F and 3.18) extracted from ASTER and Landsat images (Figure 3.16 D & E, respectively) by using automatic lineament extraction approach. The overlapping lineaments make up 11025466 m total length and correspond to 72% of the lineaments extracted from ASTER image and 54% of the lineaments extracted from Landsat image.

The final step includes the application of same procedure to the resultant maps produced from manual and automatic lineament extraction approaches (Figure 3.16 C & F, respectively) By this process, the final lineament map is obtained (Figure 3.16 G and 3.19). The total length of the lineaments in the final map is 2651053 m and makes up 45% of the lineaments obtained from manual and 24% of the lineaments obtained from automatic approach.

The SRTM data and aerial photographs are excluded in this process due to their spatial resolutions. SRTM data provides more regional information whereas aerial photographs supply more local information, which are not coincide with information extracted ASTER and Landsat TM.

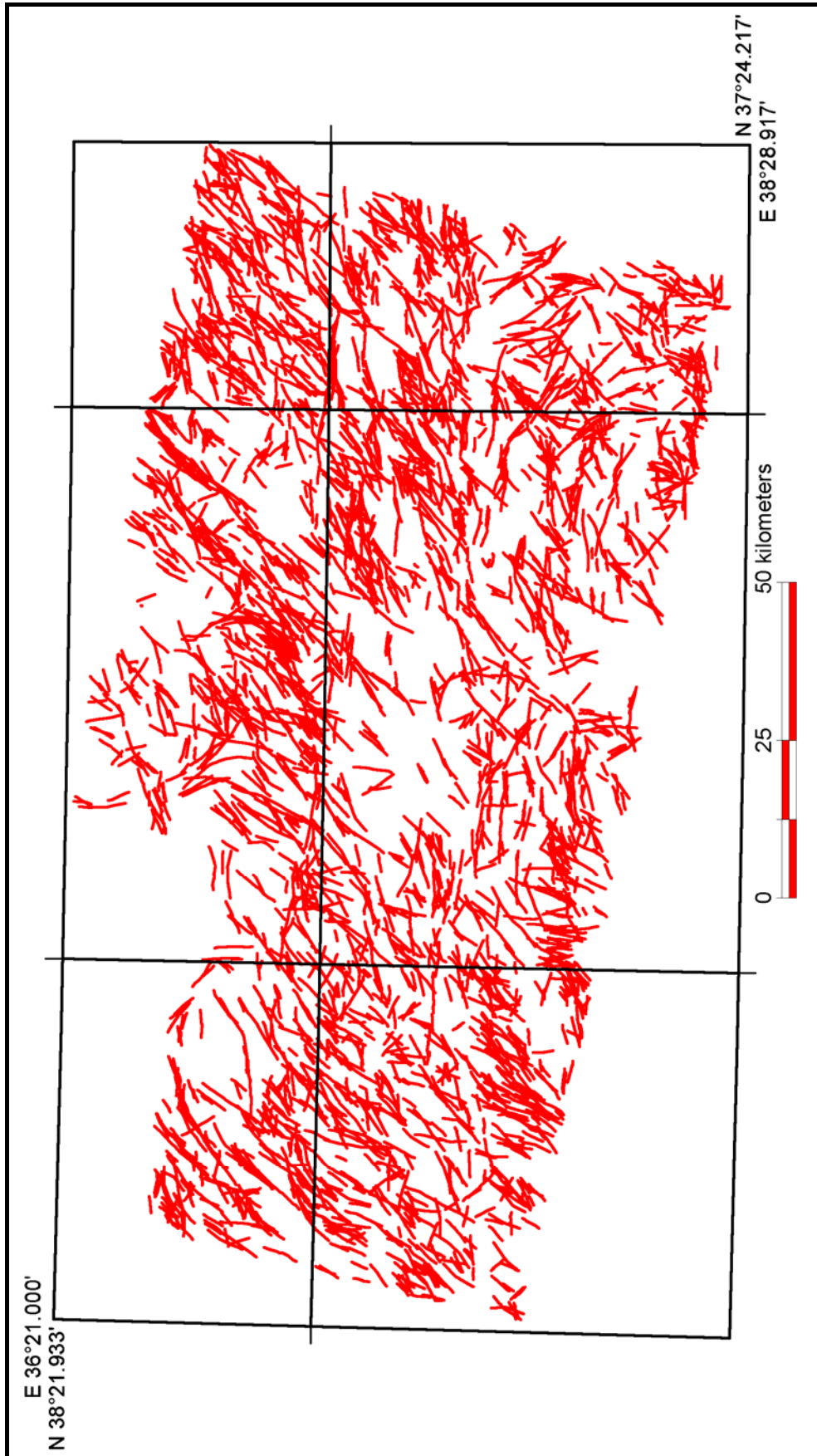


Figure 3.18 Resultant map obtained from overlaying of the lineament map obtained from ASTER and Landsat TM using automatic approach.

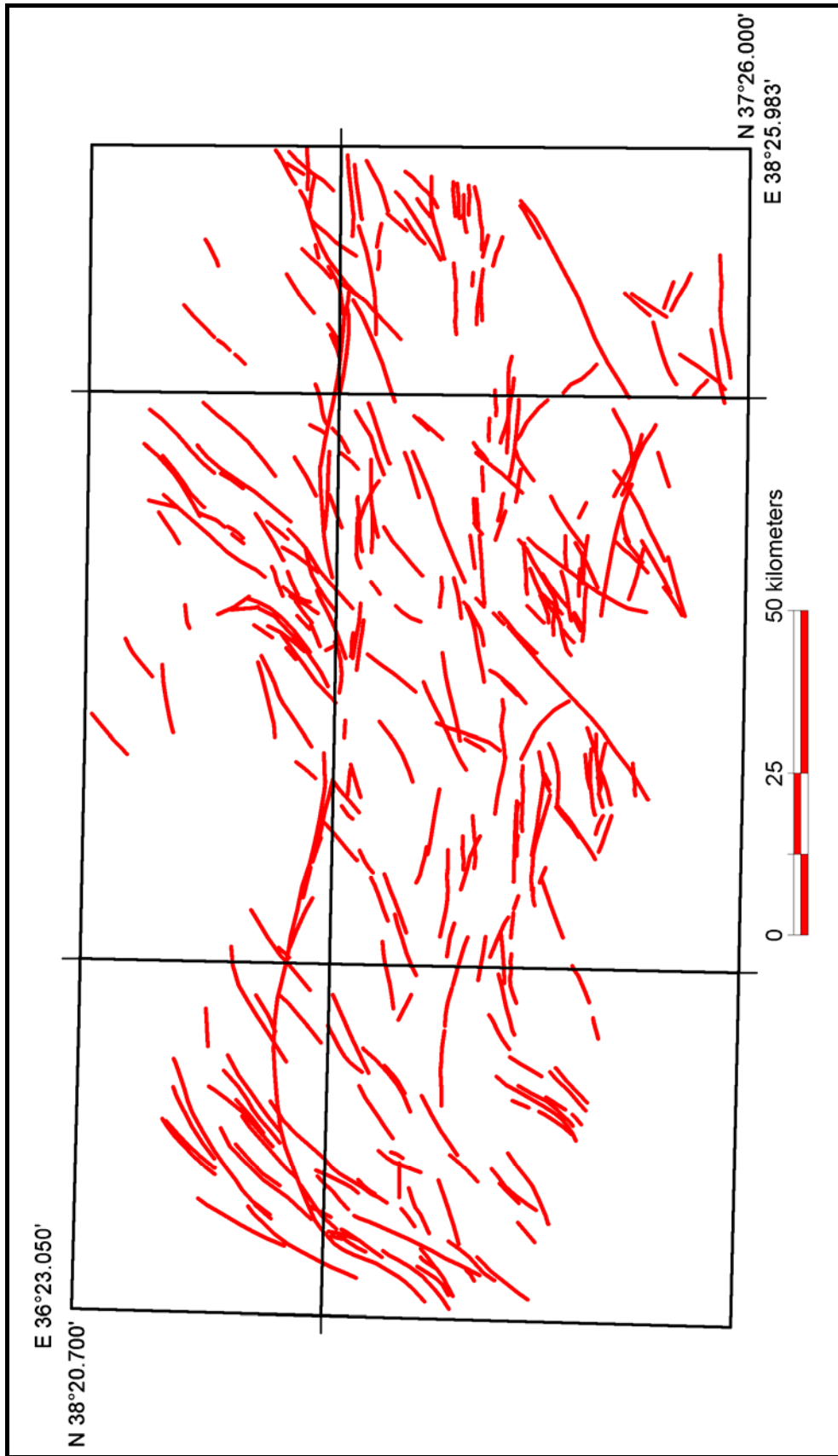


Figure 3.19 Final lineaments map obtained from overlaying of the resultant maps of manual and automatic methods.

## CHAPTER 4

### REMOTE SENSING MANIFESTATIONS OF THE SÜRGÜ FAULT ZONE

This chapter describes the remote sensing characteristics of the SFZ in order to understand its role and the mechanism over the area of interest. This chapter consists of three main sections: The first section provides the characteristics of the SFZ obtained only from the ASTER data alone. The second section contains the information obtained from the Stereographic Aerial Photographs. The final section is designed to make a comparison between these two data sources in various aspects.

The mostly observed kinematic indicator and morphological features along the SFZ include pressure ridge, lithological juxtapositions, shutter ridges (displaced transverse ridges), abrupt changes in elevation (sudden relief change) and systematically deflected streams. In addition to that, within the interpreted fault blocks, a number of well-arranged (systematic) linear features which are interpreted as joint sets are also observed within and just outside of the fault zone.

#### 4.1 ASTER

Detailed studies performed over the ASTER data show that several kinematic indicators are present along the SFZ. The most evident one is the linearly arranged ridges that are interpreted to be pressure ridges produced by compressional bends or stopovers along the main course of the SFZ (Figure 4.1). The orientation of the pressure ridge clearly defines that the strike of the SFZ is about E-W direction. It extends from Çelikhan Basin and controls the northern margin of the Kozaklı Basin. Within the zone of pressure ridges a number of deflected streams with apparent dextral off-set are also observed (Figure 4.2). Observed deflections in the stream courses are more than 2 km.



Figure 4.1 ASTER image (band combination; R:3, G:2, B:1) showing pressure ridges within an anastomosing en echelon pattern of faults (yellow lines).

It is interpreted that the southwards flowing streams are off-set dextrally in accordance with the movement direction of the fault zone. It is further interpreted that the upstream side of the streams flow down until it meets its downstream continuation. This results in deflection and capturing (upstream and downstream sections belongs to different streams) of the streams, which result in a very complex network of streams. Considering that the present drainage network is set after Pleistocene post glacial period (i.e. Holocene, last 10k years), minimum cumulative dextral off-set of the SFZ during the Quaternary might be more than 2 km.



Figure 4.2 ASTER image (band combination; R:3, G:2, B:1) showing dextrally displaced streams along the SFZ between Çelikhan and Sürgü

Similarly, displaced streams are also detected at NW of the Nurhak and E of Derbent (Figure 4.3). In this area, the deflection pattern is not as simple and regular as the deflections in the Kozaklı Basin. In this area some of the stream channels do not have appreciable downstream continuation which may be due to contortion of the drainage. This results in fanning out of stream water that does not yield a visible channel course. In this area, observed possible maximum dextral displacement is about 1 km.

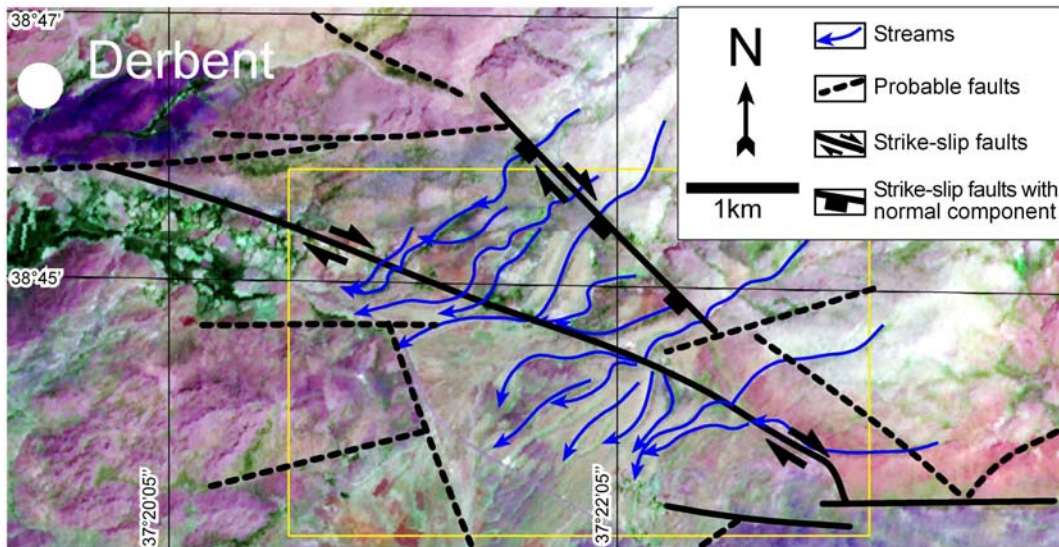


Figure 4.3 The displaced streams along the SFZ in around Derbent overlaid on ASTER image. Band combinations RGB:5,2,1 with saturation enhancement. Yellow box indicates the position of Figure 4.8.

In addition to off-set features, a number of different lithologies are juxtaposed along the very sharp trace of different segments of the SFZ (Figure 4.4). It is interpreted that the relative movements of the fault blocks result in displacements of the lithologic units on one side against the other side which results very sharp color contrast in the Satellite images due to their differing petrography and mineralogy.

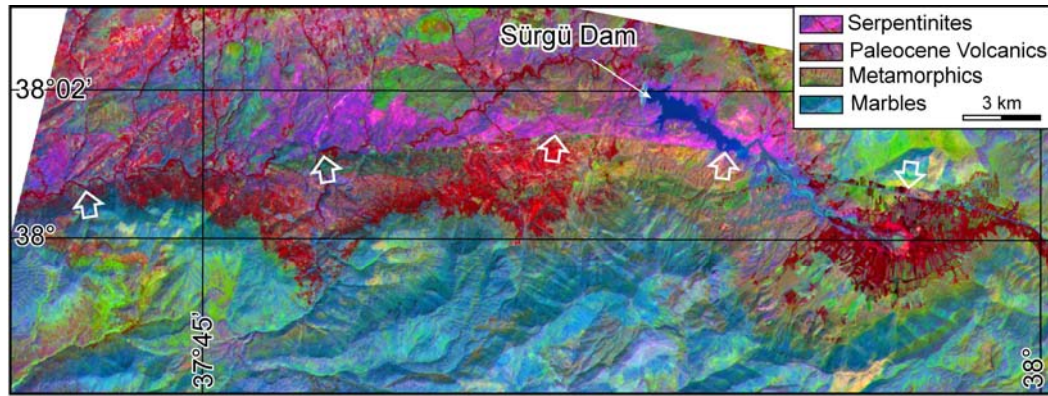


Figure 4.4 Trace Master Strand of the SFZ near Sürgü Dam indicated with white arrows and overlaid on Decorrelation stretched ASTER image. Band combinations; RGB:4,2,1. Note very sharp trace of the Master Strand of the SFZ.

In the southern margin of the Kozaklı Basin, it is observed that there are a number of NE-SW oriented blocks delimited by very prominent fault traces and the Kozaklı Basin has a stair case geometry. It is interpreted that the staircase geometry is due to clockwise rotation of these fault blocks which is originated by domino-style faulting similar to book-shelf mechanism (Wernicke and Burchfield 1982). This rotational phenomenon is associated with right lateral strike slip motion of the SFZ. The faults between blocks have the opposite sense of shear (sinistral) than shear zone itself (dextral) (Figure 4.5).

At the western part of the study area, the traces of the SFZ (SFZ) are recognized easily due to abrupt changes in elevation such as scarps or cliffs (Figure 4.6). In this area, high topography of southern block abuts the alluvial plain of the Göksun and Elbistan basins.

The western termination of the SFZ is bended southwards. According to Biddle and Christi-Blick (1985) and Sylvester (1988), such bends in dextral strike-slip systems should have a compression component and are classified as restraining bend which is confirmed during the field studies (see chapter 5).

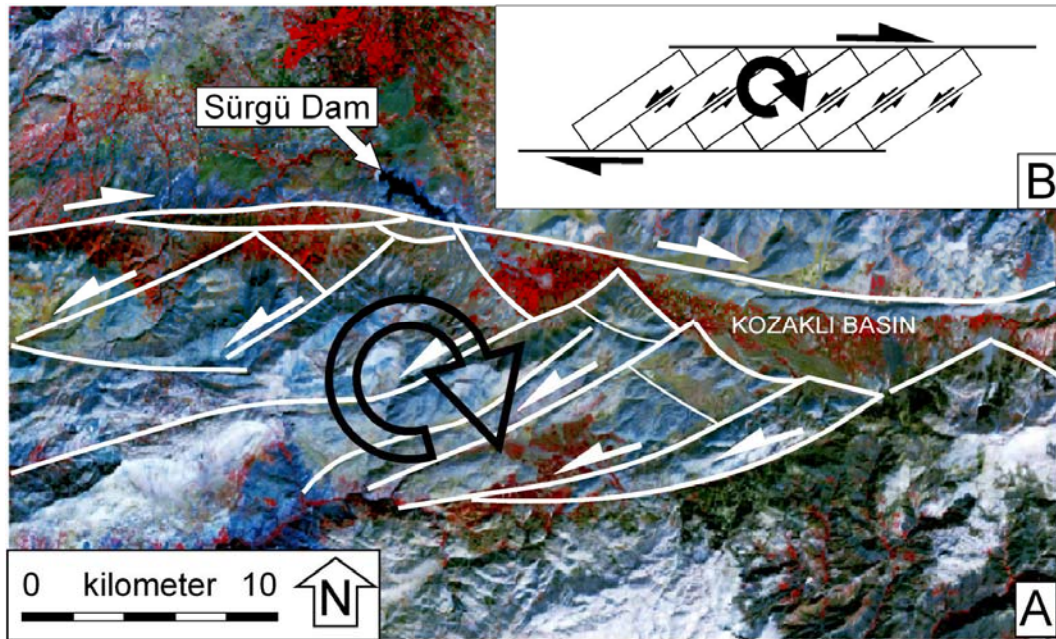


Figure 4.5 A) Fault blocks developed in the southern side of the SFZ overlaid on the ASTER image (band combination RGB:3,2,1). B) Domino style (bookshelf) faulting proposed to explain the development of fault blocks along the SFZ. Note sinistral movement (half arrows) of clockwise rotating blocks (circular arrows) within dextral system (SFZ). Note also that all faults are not indicated for the sake of simplicity.

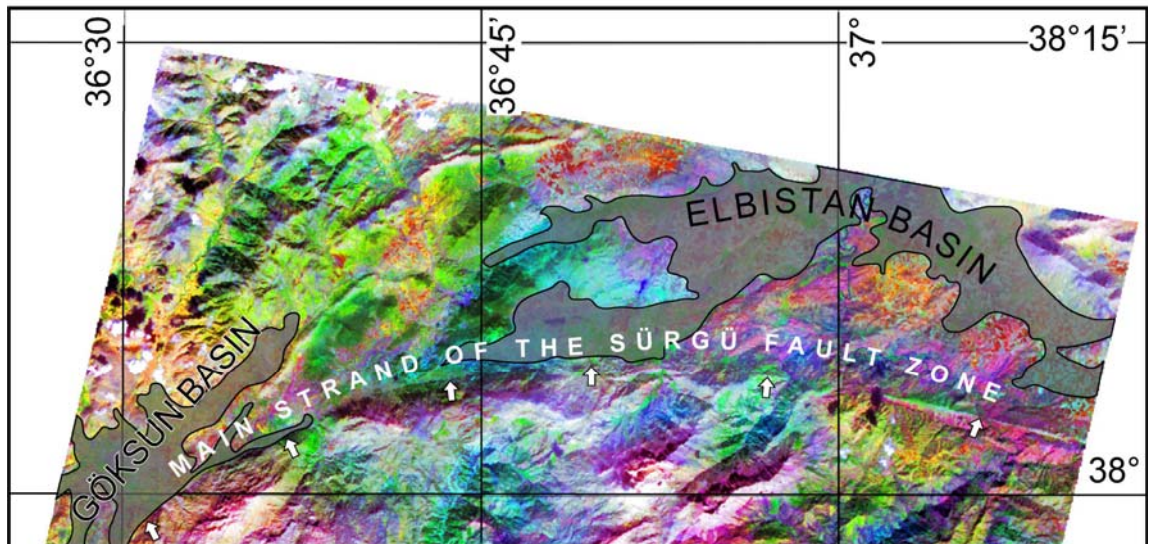


Figure 4.6 Subset of an ASTER image depicting a very sharp trace of the SFZ (for the sake of clarity fault trace is not delineated but indicated with arrows). The image is produced by DS and PCA. Band combination; RGBI:5,3,1, intensity is PC-1.

## 4.2 Stereographic Aerial Photographs

In the aerial photographs, similar geomorphological features observed on the ASTER images are also observed. Since the aerial photographs have higher ground resolution and relief information, relatively diffuse and unrecognizable features are detected and delineated more precisely. Similar to ASTER imagery, the common morphologic features detected in the aerial photographs are as follows; aligned ridges which were previously interpreted as pressure ridges, deflected stream courses, sudden relief changes, lithological juxtapositions, etc. (see Figure 4.7, 4.8 and Figure 4.9).

The most striking differences between the results of ASTER images and the aerial photographs is that the pressure ridges and the deflected streams in the northern margin of the Kozaklı Basin are interpreted precisely in the aerial photographs (Figure 4.7). It is observed that the belt of pressure ridges can be divided into a number of small blocks by NE-SW striking en echelon faults with sinistral off-set and displays an anastomosing pattern. It is interpreted that these blocks are also rotated clockwise within the dextral system as discussed previously.

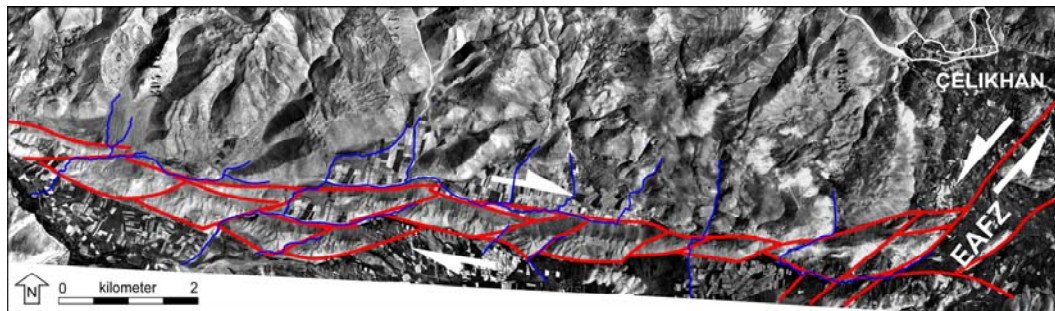


Figure 4.7 Aerial photo showing pressure ridges within an anastomosing en echelon pattern of faults (red) and dextrally displaced stream courses (blue). EAFZ: East Anatolian Fault Zone. Note that all the streams flow southwards.

In addition to the northern margin of the Kozaklı basin, the deflected streams in the E of Derbent and NW of Nurhak are also ore precisely interpreted (Figure 4.8). In this area, amount of deflection is also about 1 km as observed on the ASTER images.

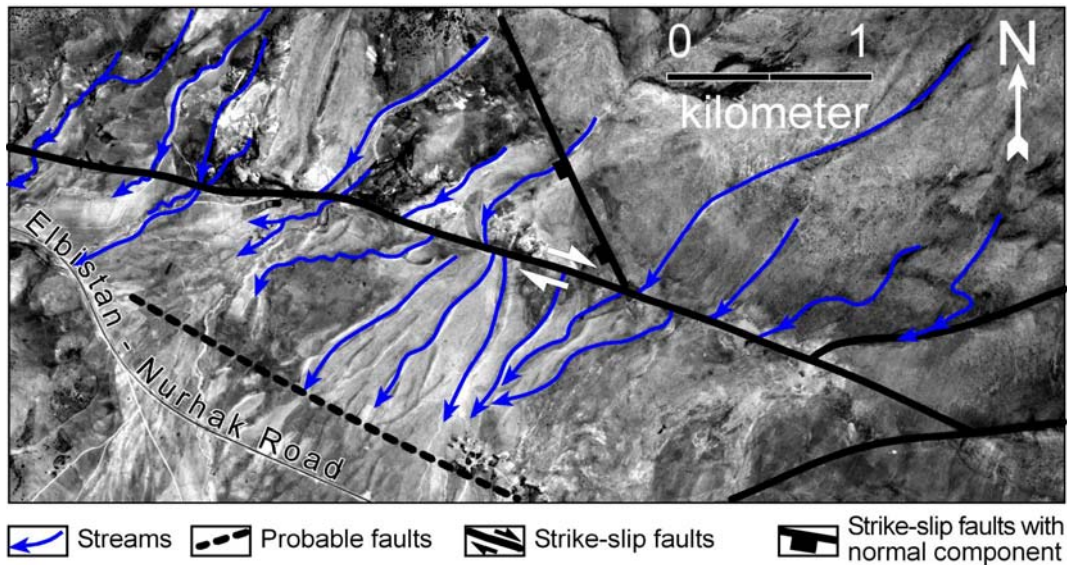


Figure 4.8 Deflected streams in E of Derbent and NW of Nurhak overlaid on the aerial photo. (See Figure 4.3 for its location)

Similarly, the sudden elevation change and abutting of southern block of the SFZ to the alluvial plain of Göksun Basin are better interpreted (Figure 4.9). In this area, north dipping fault scarp is very sharp and easily recognizable even with unaided eye.

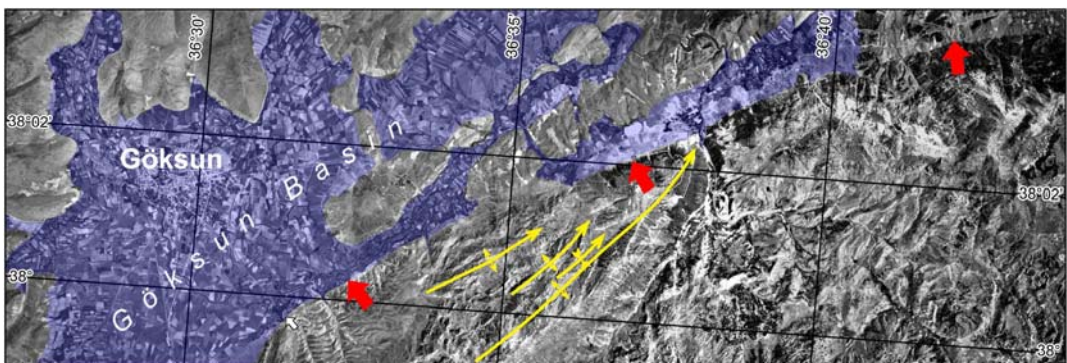


Figure 4.9 Aerial photo showing western part of the study area. Main Strand of the SFZ is dipping northwards and is indicated with red arrows. Singly plunging anticlines and synclines are indicated with yellow lines.

During the detailed studies performed over the aerial photographs, a number of NE-SW trending en-echelon folds are also observed (Figure 4.9). Since these

folds were developed within pre-Neogene units which may be developed prior to the development of the SFZ, they are not taken into consideration although they indicate dextral movement which is also supportive information for the dextral movement of the SFZ.

## **CHAPTER 5**

### **GROUND TRUTHING: FIELD OBSERVATIONS AND PALAEOSTRESS STUDIES**

This chapter is dedicated to the field study which is performed for verification and truthing of the information extracted from the remotely sensed imagery in various scales and to collect extra information related to the geometries and kinematics of the faults distribution over the study area. The chapter comprises two main sections; 1) the field observations for ground verification of the interpreted lineaments and 2) fault slip data collected in the field and used to construct palaeostress configurations that help to understand the deformation mechanism and fault kinematics of the region.

#### **5.1 Field Observations**

The remote sensing studies always include field verification of the remotely sensed data. For this purpose, ground truth is carried out to verify and correlate observed geologic and geomorphological features on the images on the ground. Before the field verification all the information extracted from the remotely sensed data and literature information is gathered and integrated. Then, test areas are selected before going into field to save time and money which is one the advantages of the remote sensing.

The field studies were concentrated mainly to the SFZ proper, rather than whole study area in line with the main purpose of this study. During field studies, almost all the delineated lineaments within and around the SFZ are visited where they are pre-determined (using remote sensing) to be best observable and the kinematic indicators such as deflected streams, pressure ridge (Figure 5.1), abrupt changes in elevation (Figure 5.2) and juxtapositions of different lithologies (Figure 5.3), which are explained in chapter 4, are confirmed in the field. In

addition to these fault slip data are collected in selected reference sites which were determined previously using remote sensing data.



Figure 5.1 General view of Kozaklı Basin and the pressure ridges in its northern margin PR. Pressure ridge (view to NE).

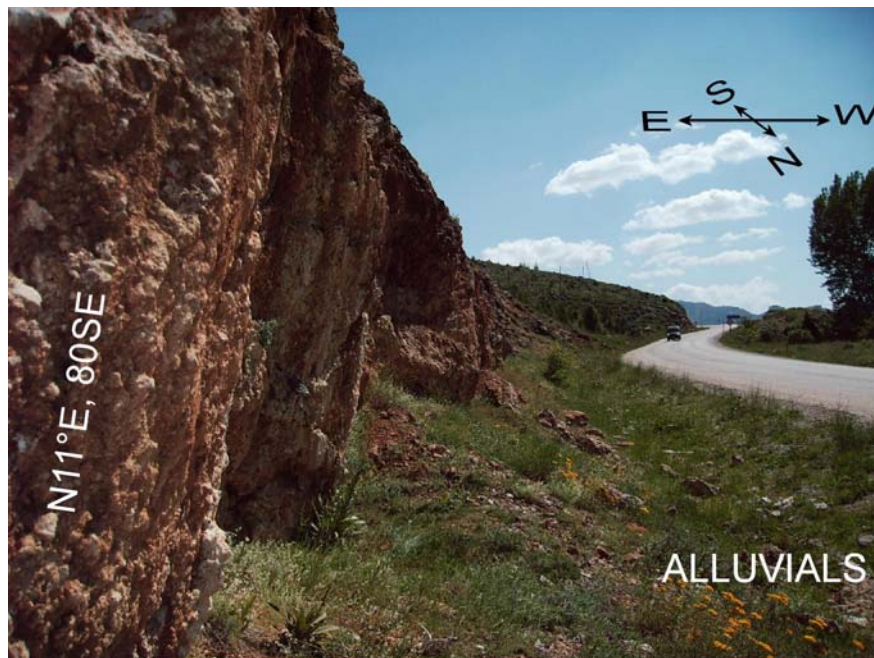


Figure 5.2 Abrupt elevation change and cataclasites developed along the westernmost end of the SFZ around Göksun (Site-1, see Appendix A for its location). Note reverse component of the fault. View to S.

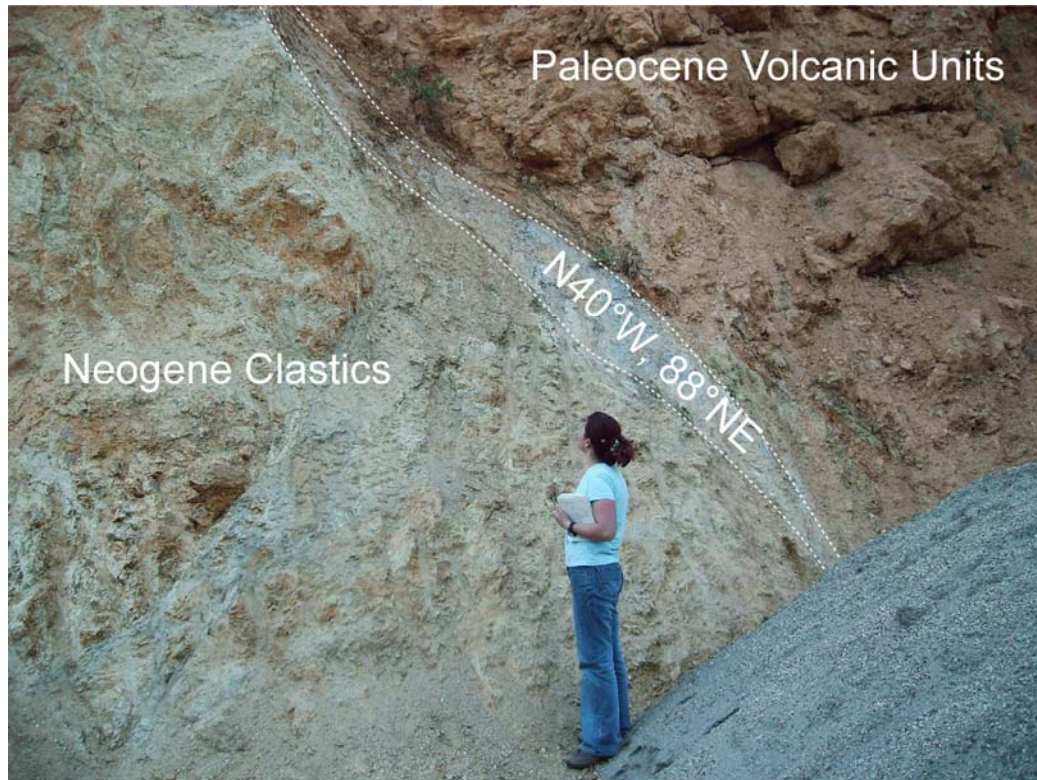


Figure 5.3 Stratigraphical juxtaposition around Derbent (Site-12, see Appendix A for its location). View to N. Note reverse component of the fault.

During the field studies, various compressional and extensional structures are also observed in different locations along the fault zone. Slickensided surfaces (Figure 5.4), block tilting, aligned mineral water springs, narrow linear valleys (Figure 5.5), phacoid structures (Figure 5.6), fault rocks (fault breccia, cataclasite, fault gouge and shear zones, Figure 5.7), and conjugate faults (Figure 5.8) are observed. All these information together with collected fault slip data are used to analyze the kinematic development and palaeostress history of the SFZ.



Figure 5.4 Slickensides developed in the western end of the SFZ around Göksun (Site-1, see Appendix A for its location).



Figure 5.5 E-W trending linear valley developed along the Kurucova Segment of the SFZ. View to E from Site-15 (see Appendix A for its location).



Figure 5.6 Phacoids developed within a sinistral fault developed between the pressure ridges in the northern margin of the Kozaklı Basin (Site-15).

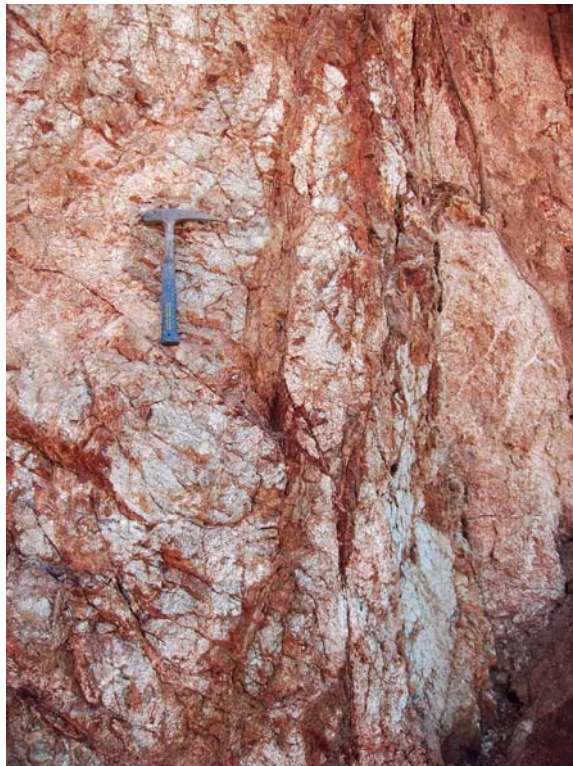


Figure 5.7 Shear zones developed within the SFZ around Site-3 (see Appendix A for its location). View to W. It is a strike-slip shear zone with reverse component. Orientation of the zone is N70°E, 80°SE.



Figure 5.8 Conjugate faults developed in Paleocene Volcanic units within the SFZ around Sürgü. View to E, location: Site-8 (see Appendix A for its location).

## 5.2 Palaeostress Studies

From 19 sites, 245 fault slip data are collected. In collecting the data, the strike of the fault plane, its dip and rake of the slickensides and sense of the movements are noted. The samples are collected from all units exposed in the study area. Those are Paleozoic to Mesozoic marbles, and metamorphics, Late Cretaceous ophiolites and ophiolite related units, Paleocene volcanic and clastic units, and Neogene sedimentary and volcanic units.

Palaeostress configurations are constructed using Angelier's software (Angelier, 1988) and presented in lower hemispheric, equal area projections. After the analysis of the data it is found that approximately 3.26 % of the data was spurious which makes up 8 faults. Remaining 237 faults yielded reasonable stress configurations which is given Figure 5.2. The evaluation of the results is performed in discussion section.

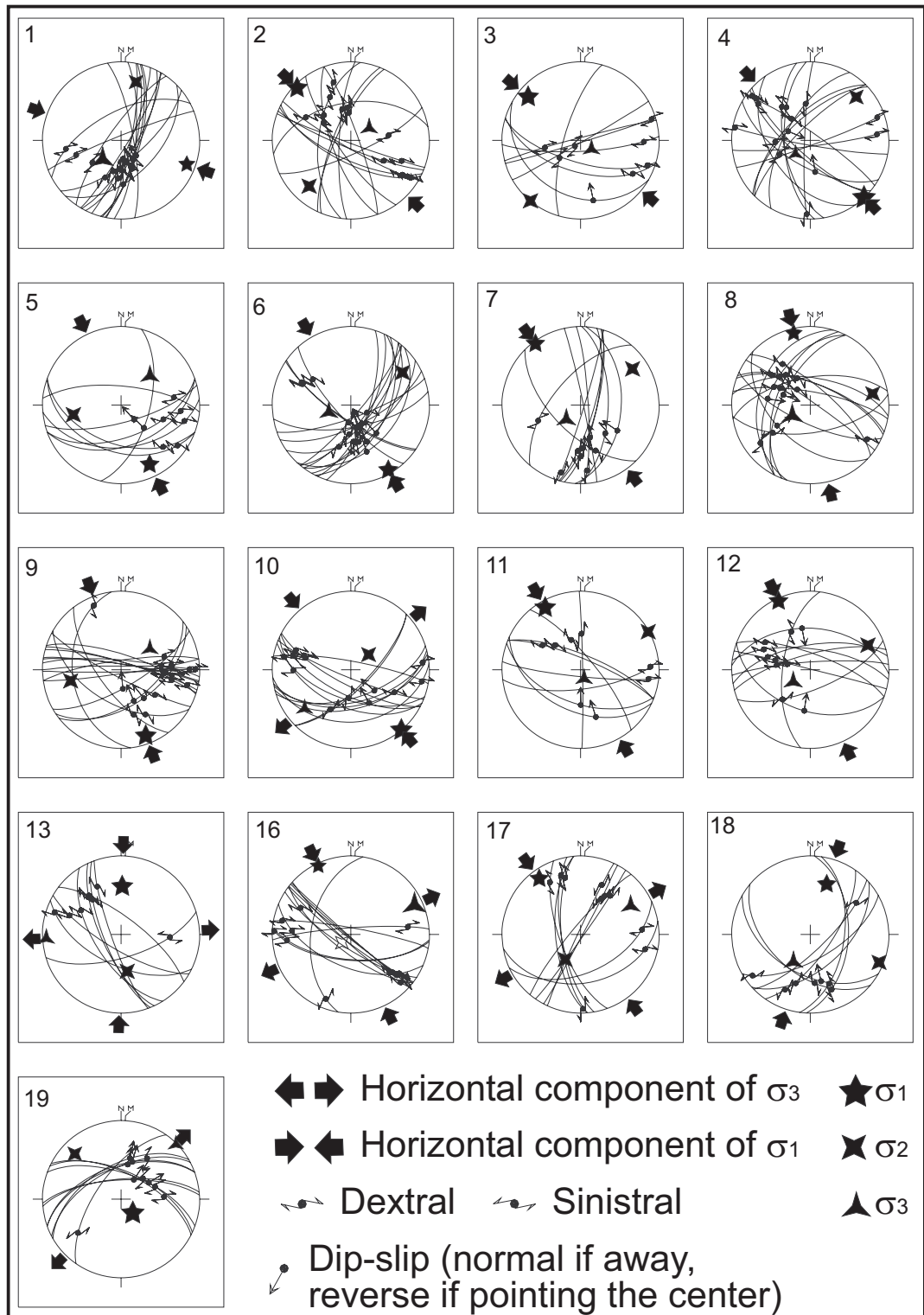


Figure 5.9 Cyclographic traces of fault planes and constructed palaeostress configurations for each site. Lower hemisphere, equal area projection. See Appendix A for measurement locations.

## **CHAPTER 6**

### **DISCUSSIONS**

In this part, first the advantages and disadvantages of various imageries (data) and the methods that are used in this study followed are discussed.

#### **6.1.1 Data**

The SRTM data has the least ground resolution (90 m) among the data sets used in this study. Because of this, it is suitable for delineating major (large scale) regional lineaments. In addition to this, it is very handy for delineating lineaments that are oriented in different directions by use of changing illumination direction in making shaded relief images. Shaded relief images are produced by manipulating the illumination source in azimuth and dip (elevation, in degrees). One of the advantage of the SRTM is that it is blind to ground cover types of some extent, i.e. the lineaments can be detected and delineated even they are covered by vegetation. In the case of very high trees, this property is negatively affected, since they may alter the obtained topographical information. Moreover, extraction of the lithologic information using the SRTM data is not possible as it lacks spectral information.

Landsat-5 (TM) imagery has higher spatial resolution (30 m) with respect to the SRTM. It means that an area covering 1 pixel in SRTM data is represented by 9 pixels in TM data. Therefore, it provides more detailed information. In addition to this, multispectral characteristics of the TM data make it functional for lithological and mineralogical (to some extent) discrimination. It has superiority to perform lithologic discrimination using different band combinations, and extra channels that can be produced by various image analysis techniques such as PCA and DS techniques. Other advantage of TM over other satellite based imaging is that it is

one of the oldest sensor by which it is well calibrated and very robust imaging system. Having only 7 bands and large swath makes it easy to handle and process with respect to ASTER imagery.

Spatial resolution of the ASTER VNIR data (15 m) is higher than the Landsat TM and the SRTM data. Therefore, the morphological markers are extracted from the images easily. Lineaments may be extracted by interpretation of these morphological signatures although there is no significant fault trace. These make the detailed regional lineament maps possible. However, using the SWIR bands of the ASTER data which have 30 m spatial resolution does not provide any advantages with respect to using Landsat TM data. Besides, ASTER data have some limitations in particular type of studies due to lack of blue band.

In addition to these three data sets, 1:35,000 scale aerial photographs are also used in this study. It has the highest spatial resolution among the data used. The capability of stereographic view of the aerial photographs makes it a powerful tool for detecting earth features in their spatial context. It complements most of the imaging systems and bears information for understanding of the local (very small scale) phenomena. However, the aerial photographs have some limitations. First, it has lower temporal resolution which makes some kind of studies impossible to perform, e.g. very frequent change detection studies. Secondly, large scale geologic features, which extend out of the photo pair coverage, can be detected but most of the time missed due to the lack of continuity in the successive photo pairs. Thus, the regional information is obtained by using the subsegments or mosaicing, which makes some regional information omitted. Thirdly, extraction of the lithologic information in the aerial photographs depends on the tonal variation which is subjected to wide variation (which strongly dependent on type of film used, exposure timing, paper quality etc.) which may vary picture to picture. In this context, relative tonality is mentioned. In addition to these drawbacks, working with the aerial photographs is a time consuming and tedious process. For example, this process took 5 weeks in this study.

All of the data sources used in this study are complementary to each other, so that drawbacks of one type of imagery are overcome by the other.

### **6.1.2 Methods**

In this study three different types of lineament extraction procedures were followed. These are 1) manual, 2) semi automated, and 3) automated lineament extraction techniques.

The manual lineament delineation depends on expert knowledge. Therefore, the resultant lineament map will change according to knowledge of the analyst (subjectivity).

During the visual interpretation of the lineaments, there may be obscured lineaments additional to recognized ones. Nevertheless, visual interpretation is still the most reliable method for geological lineament analysis because human perception can discriminate geological lineaments from others (e.g. roads, crop-field boundaries) using contextual information.

Semi automatic and automatic lineament delineation is developed for minimizing the subjectivity of analyst and saving time. However, non-geological and artificial lineaments may be added to the final lineament map due to the nature of filters used. For example, after the lineaments are overlaid with color composite of the satellite imagery, it is noticed that drainage networks, ridges and artifacts, such as roads and field boundaries etc., are also extracted as lineaments in this method.

## CHAPTER 7

### RESULTS AND DISCUSSIONS

In this thesis, a new set of information that is used to explain the kinematics of the SFZ is extracted from the remotely sensed data combined with the field observations. Eight lineaments maps are prepared using ASTER, Landsat and SRTM images and Aerial photographs using manual, semi automatic and automatic approaches. The results of these methods and imagery are given in Table 7.1.

Table 7.1 Summary statistics of the lineaments obtained using various data sets and methods.

| Length (m)  | SRTM    | LANDSAT 5 (TM) |                |           | ASTER   |                |           |
|---|---------|----------------|----------------|-----------|---------|----------------|-----------|
|   | Manual  | Manual         | Semi Automatic | Automatic | Manual  | Semi Automatic | Automatic |
| Max   | 36411   | 38677          | 36173          | 10143     | 38681   | 22381          | 10417     |
| Min   | 8.081   | 1.645          | 2.069          | 0.194     | 0.355   | 3.717          | 0.243     |
| Average   | 3842    | 3668           | 4783           | 1096      | 2483    | 3419           | 1201      |
| Sum   | 6385972 | 7117255        | 6251759        | 20225156  | 7705436 | 7934338        | 15103904  |
| Number  | 1662    | 1940           | 1307           | 18444     | 3103    | 2320           | 12570     |
| The area covered by the ASTER imagery is taken as a reference for the statistical analyses. . |         |                |                |           |         |                |           |

Among these, the lineament maps produced from ASTER and Landsat imagery by only manual and automatic lineament extraction methods are used to produce two resultant (intermediate product) lineament maps both for the manual and automatic approaches by overlying operation. Then, these intermediate products

are used to obtain the final lineament map by following the same procedure. The summary statistics of these maps is given in Table 7.2.

As seen in tables 7.1 & 7.2, the number and the length of the lineaments using automatic method is more than the lineaments obtained by manual method. This relationship is possibly due to the fact that the automatic lineament approach does not discriminate man made features during the analysis. This increases the total number and length of the lineaments. This explains possibly why the total number and total length of the lineaments obtained from manual method is less than other methods.

Table 7.2 Summary of the intermediate products and the final lineament map.

| <b>Step 1</b>                            |                  | <b>ASTER</b>            | <b>Landsat (TM)</b>        |
|--|------------------|-------------------------|----------------------------|
| <b>Intersection Manual</b>               | Total Length (m) | 5,938,825               |                            |
|  | Number           | 2114                    |                            |
|  | Percentage (%)   | 77                      | 83                         |
| <b>Step 2</b>                            |                  | <b>ASTER</b>            | <b>Landsat (TM)</b>        |
| <b>Intersection Automatic</b>            | Total Length (m) | 11,025,466              |                            |
|  | Number           | 8329                    |                            |
|  | Percentage (%)   | 72                      | 54                         |
| <b>Step 3</b>                            |                  | <b>MANUAL (Product)</b> | <b>AUTOMATIC (Product)</b> |
| <b>Intersection Manual and Automatic</b> | Total Length (m) | 2,651,053               |                            |
|  | Number           | 396                     |                            |
|  | Percentage (%)   | 45                      | 24                         |

On the other hand, the percentages of the overlapping lineaments obtained from manual method are higher than the automatic approach. This is because of the fact that during manual interpretation process, by default, the man made features are ignored and most likely geological lineaments are delineated.

The lineament maps are also evaluated by constructing rose diagram which illustrates dominant trends (Appendix A). It shows that the lineaments are mainly oriented NE-SW direction which coincides with the orientation of the EAFZ. It means that the most of the lineaments in the region are developed under the same stress conditions that gave way to the EAFZ. The field studies confirmed that most of these lineaments are sinistral in nature as EAFZ does. Another lineament set that is aligned E-W is also observed. This trend is parallel to the general trend of the SFZ and the field studies confirmed that most of them are generally dextral strikes-slip faults with reverse component of slip. The other most prominent set occurs in NNE-SSW direction and is parallel to the trend of the Malatya Fault Zone. During the field studies, it is observed that the faults in this trend are generally sinistral in nature.

In addition to this, the region is divided into four subsets in order to see if there is any local variation in the orientations of the lineaments (Appendix a); and it is observed that there is no major change in the orientations of the detected lineaments. This information indicates that the region is subjected to relatively homogeneous strain so that the deformation is not constrained into discrete zones.

One of the most important conclusions of this thesis is that, the SFZ, which is the main concern of this study, is a dextral strike-slip fault zone with a reverse component of as indicated by morphological features (e.g. deflected streams along the Kuruçova Segment). This conclusion challenges almost all the previous works (especially Perinçek *et al.* 1987; Taymaz *et al.* 1991; Şaroğlu *et al.* 1992) which claimed that the “so called” Sürgü Fault is a sinistral fault zone with and locally without reverse component.

The other conclusions are as follows;

- in the SFZ block rotations about vertical axes are very common. They resulted in the stair case geometry of the Kozaklı Basin;
- a number of morphological features very common to strike-slip faults are developed within the SFZ. These are pressure ridges, deflected stream courses, juxtaposition of different lithologies, tilted terraces, mineral water springs etc;

- the palaeostress measurements along the Kurucova Segment indicate the SFZ has normal component of slip which is caused by the block rotations;
- it is noticed that there is an offset between the Kurucova Segment and the Ericek-Derbent Segment of the SFZ. It is thought that this offset is resulted from the sinistral Malatya Fault Zone, contrary to Şaroğlu *et al.* (1992) who considered these two segments as two different faults;
- palaeostress analyses based on 245 fault slip data additional to the analyses of several other kinematic indicators including conjugated fractures, tension and hybrid fractures, drag folds support the proposed interpretations i.e. the SFZ is a dextral strike slip fault zone.
- the dip-slip component of the fault is controlled by its geometry, e.g. the Main Strand of the SFZ, in the west near Göksun, has very strong reverse component since the fault has southwards anticlockwise bend (left), while in the east near Sürgü and Kozaklı Basin, it has normal component of slip coupled with block rotation and clockwise (right) single bend (Figure 7.1).

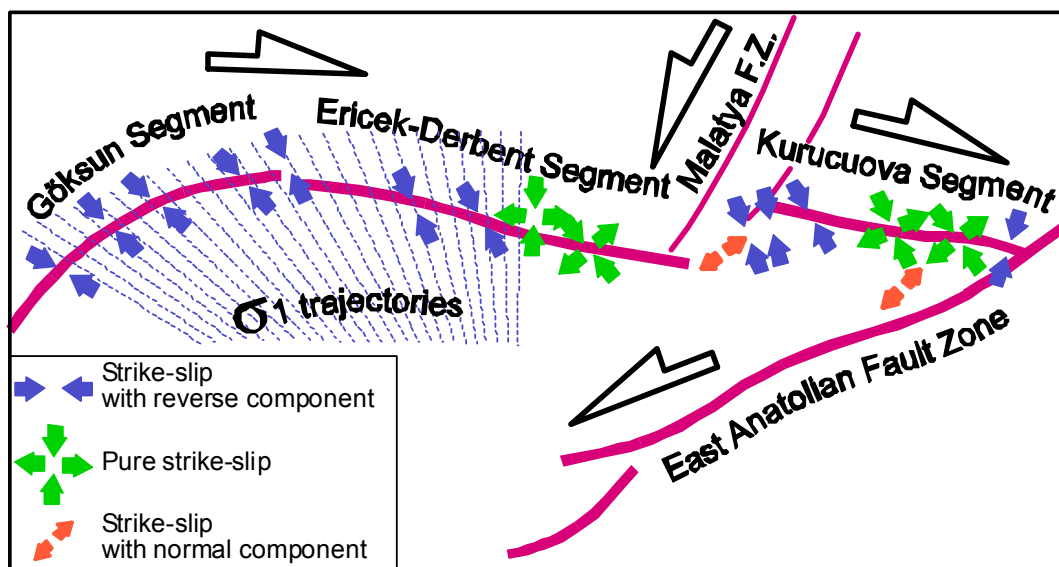


Figure 7.1 Simplified map showing the segments of the SFZ and orientation of horizontal components of constructed palaeostress configurations. Note 1) rotation of major principal stress as the trend of the fault changes (trajectories), 2) domination of strike-slip component over dip-slip from W to E and 3) domination of NE-SW extension in the east, S of Kurucova Segment, 4) position of Malatya Fault Zone.

- the palaeostress analysis indicates the stress tensors rotates as the geometry of the master strand changes while  $\sigma_3$  is kept fixed (Figure 7.1).
- presence of displaced (deflected) stream courses, tilted terraces, water springs along the fault zone observed during the field study point out that the SFZ is still active. In addition to these, three major earthquakes occurred in 1964 June 14 ( $M_s=5.7$ ), 1986 May 5 ( $M_s=5.9$ ) and 1986 June 6 ( $M_s=5.6$ ) within the SFZ. The focal mechanism solutions of these earthquakes performed by the Taymaz *et al.* (1991) indicate that the SFZ is a sinistral strike-slip fault zone. However, the resolved fault planes do not correspond to the planes of the SFZ and two of them are located within the intersection of Malatya Fault Zone and the other one is located in the junction of the EAFZ. Therefore, they do not necessarily belong to SFZ.
- Observed maximum dextral cumulative off-set along the SFZ is 2 km.

## **CHAPTER 8**

### **RECOMMENDATIONS**

In this study, most of the aspects related to the SFZ are covered, however, there are some incomplete or conflicting points with the previous works. In order to solve these problems, following works can be performed in the future.

1. It is known that due to poor knowledge about the crustal structure and travel velocities of earthquakes, as high as 30 km mislocations may occur in the positioning of the earthquakes. Therefore, a re-location study may be performed for the 3 devastating earthquakes in the region.
2. A very extensive field study may be performed to check all the delineated lineaments
3. A palaeomagnetic study may be performed to test the proposed block rotation models
4. Higher resolution DEMs may be obtained for more detail.

## REFERENCES

- Abrams, M., 2000, The Advanced Spaceborne Thermal Emission and Reflection Radiometer (ASTER): Data Products for the High Spatial Resolution Imager on NASA's Terra Platform. *International Journal of Remote Sensing*, 21, 847–859.
- Akhir, J. M. and Abdullah, İ., 1997. Geological Applications of Landsat TM Imagery: Mapping and Analysis of Lineaments in NW Peninsula Malaysia. <http://www.gisdevelopment.net> visited on 24.11.04.
- Akman, A.Ü. and Tüfekçi, K., 2004. Determination and Characterization of Fault Systems and Geomorphological Features by RS and GIS Techniques in the WSW Part of Turkey. *XXth ISPRS Congress, Istanbul*.
- Arlegui, L. E., and Soriano, M. A., 1998. Characterizing Lineaments from Satellite Images and Field Studies in the Central Ebro Basin (NE Spain). *International Journal of Remote Sensing*. 19 (16), 3169-3185.
- ASTER GDS, 2005.  
[http://www.gds.aster.ersdac.or.jp/gds\\_www2002/index\\_e.html](http://www.gds.aster.ersdac.or.jp/gds_www2002/index_e.html) visited on 24.05.05.
- Biddle, K.T. and Christie-Blick, N., 1985. Deformation and Basin Formation Along Strike-Slip Faults. in: Biddle, K.T. and Christie-Blick, N. (eds) *Strike-slip deformation, basin formation and sedimentation Spec. Publ. Soc. Econ. Paleont. Miner.* No. 37. 1-45.
- Bozkurt, E., 2001. Neotectonics of Turkey-a Synthesis. *Geodinamica Acta*. 14, 3-30.
- Canas, A. A. D., Barnett, M. E., 1985. The Generation and Interpretation of False-Color Composite Principal Component Images. *International Journal of Remote Sensing*. 6 (6), 867-881.
- Cooper, G.R.J., 2003. Feature Detection Using Sun Shading. *Computers and Geoscience*. 29, 941-948.

- Cross, A., Wadge, G., 1988. Geological Lineaments Detection Using The Hough Transform, *IGARSS'88 Proceedings Edinburgh, Scotland*, pp. 1779-1782.
- Dewey, J.F., Hempton, M.R., Kidd, W.S.F., Saroglu, F., Şengör, A.M.C., 1986. Shortening of Continental Lithosphere: the Neotectonics of Eastern Anatolia – a Young Collision Zone. *Collision Tectonics, Geological Society Special Publication*. 19, 3-36.
- Eurimage, 2005. <http://www.eurimage.com> visited on 24.05.05.
- Fu, B., and Lin, A., 2002. Spatial Distribution of the Surface Rupture Zone Associated with the 2001 Ms 8.1 Central Kunlun Earthquake, Northern Tibet, Revealed by Satellite Remote Sensing Data. *International Journal of Remote Sensing*. 24 (10), 2191-2198.
- Fu, B., Ninomiya, Y., Lei, X., Toda, S., Awata, Y., 2004. Mapping Active Fault Associated with the 2003 Mw 6.6 Bam (SE Iran) Earthquake with ASTER 3D Images. *Remote Sensing of the Environment*. 92, 153-157.
- Gillespie, A. R., 1992. Enhancement of Multispectral Thermal Infrared Images: Decorrelation Contrast Stretching. *Remote Sensing of the Environment*. 42(2), 147-155.
- Gomez, C., Delacourt, C., Allemand, P., Ledru, P., Wackerle, R., 2004. Using ASTER Remote Sensing Data Set for Geological Mapping, in Namibia. *Physics and Chemistry of the Earth*. (Article in Press)
- Henderson, D. B., Ferrill, D. A. and Clarke, K. C., 1996. Mapping Geological Faults Using Image Processing Techniques Applied to Hill-Shaded Digital Elevation Models. *IEEE Transactions*. 8, 240-245.
- Jensen, J. R., 1996. Introductory Digital Image Processing, 2nd Edition, Prentice Hall Inc., U.S.A.
- Jordan, G., and Schott, B., 2005. Application of Wavelet Analysis to the Study of Spatial Pattern of Morphotectonic Lineaments in Digital Terrain Models. A case study. *Remote Sensing of the Environment*. 94, 31-38.

- Karig, D. E. and Kozlu, H. (1990) Late Paleogene Neogene Evolution of The Triple Junction Region Near Maras, South-Central Turkey. *Journal of The Geological Society*. 147, 1023-1034.
- Karnkowski, P. H. and Ozimkowski, W., 1999. Multi-Coverage Geological Interpretation of Satellite Images: A Case Study from Selected Areas of Poland. *JAG*. 1 (2), 132-145.
- Kaymakci, N . White, S.H. and Van Dijk P.M., 2000. Paleostress Inversion In a Multiphase Deformed Area: Kinematic and Structural Evolution of The Çankiri Basin (Central Turkey), Part 1. In: Bozkurt, E., Winchester, J.A. and Piper, J.A.D. (eds.) *Tectonics and Magmatism in Turkey and the Surrounding area. Geological Society London Special Publication No. 173*. 445-473.
- Kaymakci, N. Inceöz, M. Ertepinar, P. 2005. 3D Architecture and Neogene Evolution of the Malatya Basin: Inferences for the Kinematics of the Malatya and Ovacik Fault Zones. *Turkish Journal of Earth Sciences*. (in press)
- Kocal A., Duzgun H. S., Karpuz C., 2004. Discontinuity Mapping With Automatic Lineament Extraction from High Resolution Satellite Imagery. *XXth ISPRS Congress, İstanbul*.
- Koike, K., Nagano, S. and Ohmi, M., 1995. Lineament Analysis of Satellite Images Using a Segment Tracing Algorithm (STA). *Computers & Geosciences*. 21 (9), 1091-1104.
- Koike, K., Nagano, S., Kawaba, K., 1998. Construction and Analysis of Interpreted Fracture Planes through Combination of Satellite Image Derived Lineaments and Digital Elevation Model Data. *Computers and Geosciences*. 24 (6), 573-583.
- Kozlu, H., 1987. Structural Development and Stratigraphy of Misis-Andırın Region. *7<sup>th</sup> Biannual Petroleum Congress of Turkey*. UCTEA Chamber of Petroleum Engineers-Turkish Association of Petroleum Geologist.104-116.
- Leech, D. P., Treloar, P. J., Lucas, N. S. and Grocott, J., 2003. Landsat TM Analysis of Fracture Patterns: A Case Study from the Coastal Cordillera of Northern Chile. *International Journal of Remote Sensing*. 24 (19), 3709-3726.

- Lillesand, M., and Kiefer, R. W., 1999. Remote Sensing and Image Interpretation, 4<sup>th</sup> edition, John Wiley and Sons, Inc., U.S. A.
- Lyberis, N., Yurur, T., Chorowicz, J., Kasapoğlu, E. and Gundogdu, N., 1992. The East Anatolian fault: an oblique collisional belt. *Tectonophysics*. 204, 1-15.
- Madani, A. A., 2001. Selection of the Optimum Landsat Thematic Mapper Bands for Automatic Lineaments Extraction, Wadi Natash Area, South Eastern Desert, Egypt. 22<sup>nd</sup> *Asian Conference on Remote Sensing*, 5-9 November 2001.
- Mah, A., Taylor, G.R., Lennox, P., Balia, L., 1995. Lineament Analysis of Landsat TM Images, Northern Territory, Australia. *Photogrammetric Engineering and Remote Sensing*. 61(6), 761-773.
- Muehlberger, W. R., 1981. The Splintering of the Dead Sea fault Zone in Turkey. *Bulletin of Institute of earth Sciences of Hacettepe University*. 8, 123-130.
- Muehlberger, W.R. and Gordon, M.B., 1987. Observations on the Complexity of the East Anatolian Fault, Turkey. *Journal of Structural Geology*. 9 (7), 899-903.
- NASA, 2005 <http://www.nasa.gov/home> visited on 24.05.05.
- Ninomiya, Y., 2003. Rock Type Mapping With Indices Defined For Multispectral Thermal Infrared ASTER Data: Case Studies. Remote Sensing for Environmental Monitoring, GIS Applications, and Geology II. Edited by Manfred Ehlers. Proceedings of the SPIE. 4886, 123-132.
- Novak, I. D. and Soulakellis, N., 2000. Identifying Geomorphologic Features Using Landsat-5 TM Data Processing Techniques on Lesbos, Greece. *Geomorphology*. 34, 101-109.
- O'Leary, D. W., Friedman, J. D., Pohn, H. A., 1976. Lineament, Linear, Lineation: Some Proposed New Standards for Old Terms. *Geological Society of America Bulletin*. 87, 1463-1469.
- Özgül, N., 1976. Torosların Bazı Temel Jeolojik Özellikleri. *TJK Bult.* 19, 65-78.

- Perinçek, D. and Özkaya, İ., 1981. Tectonic Evolution of the Northern Margin of Arabian Plate. *Bulletin of Institute of earth Sciences of Hacettepe University*. 8, 91-101.
- Perinçek, D. and Kozlu, H. 1984. Stratigraphy and Structural Relations of the Units in the Afşin-Elbistan-Doğanşehir region (Eastern Taurus). In: Geology of the Taurus Belt. Tekeli, O. and Göncüoğlu, M.C. (eds). General Directorate of Mineral Research and Exploration (MTA) Special Publication. 181-198.
- Perinçek, D., Günay, Y. and Kozlu, H., 1987. New Observations on Strike-Slip Faults in East and Southeast Anatolia. 7<sup>th</sup> *Biannual Petroleum Congress of Turkey*. UCTEA Chamber of Petroleum Engineers-Turkish Association of Petroleum Geologist. 89-103.
- Perinçek, D. and Çemen; İ., 1990. The Structural Relationship between the East Anatolian Fault and Dead Sea Fault Zones In Southern Turkey. *Tectonophysics*. 172, 331–340.
- Richetti, E., 2002. Structural Geological Study of Southern Apennine (Italy) Using Landsat 7 Imagery. *IEEE*. 211-213.
- Rojay, B., Heimann, A., Toprak, V., 2001. Neotectonic And Volcanic Characteristics of the Karasu Fault Zone (Anatolia, Turkey): The Transition Zone between the Dead Sea Transform and the East Anatolian Fault Zone. *Geodinamica Acta*. 14, 197-212.
- Rowan, R. and Mars, J. C., 2003. Lithologic Mapping in the Mountain Pass, California Area Using Advanced Spaceborne Thermal Emission and Reflection Radiometer (ASTER) Data. *Remote Sensing of the Environment*. 84,305-366.
- Qari, M. Y. H. T., 1991. Application of Landsat TM Data to Geological Studies, Al-Khafb Area, Southern Arabian Shield. *Photogrammetric Engineering and Remote Sensing*. 57(4), 421-429.
- Quennell, A. M., 1958. The Structural and Geomorphic Evolution of the Dead Sea Rift, Q. *J. geol. Soc. Lond*. 114, 2-24.

- Sabins, F., F., 1987. Remote Sensing: Principles and Interpretation 2<sup>nd</sup> Edition. New York, W. H. Freeman and Co. 460 p.
- Shorth, N. M., 2004. Lineaments and Fractures. Remote Sensing Tutorial. [http://rst.gsfc.nasa.gov/Sect2/Sect2\\_8.html](http://rst.gsfc.nasa.gov/Sect2/Sect2_8.html). visited on 24.11.04.
- Süzen, M.L. and Toprak, V., 1998. Filtering of Satellite Images in Geological Lineament Analyses: an Application to a Fault Zone in Central Turkey. *International Journal of Remote Sensing*. 19 (6), 1101-1114.
- Sylvester, A. G., 1988. Strike-slip Faults. GSA Bulletin. 100, 1666-1703.
- Şaroğlu, F., Emre, Ö. and Kuşçu, İ., 1992. The East Anatolian Fault Zone of Turkey. *Annale Tectonicae*. Special Issue-Supplement to Volume VI, 99-125.
- Şengör, A.M.C., Şaroğlu, F. and Görür, N., 1985. Strike-Slip Deformation and Related Basin Formation in Zones of Tectonic Escape: Turkey as a Case Study”, In: Biddle, K.T. and Christie-Blick, N. (eds.) *Strike-Slip Deformation Basin Formation and Sedimentation*. Society of Econ. Palaeo. and Miner. Spec. Publ. No. 37, 227-264.
- Taymaz, T., Eyidoğan, H., Jackson, J., 1991. Source Parameters of large earthquakes in the East Anatolian Fault Zone (Turkey). *Geophys. J. Int.* 106, 537-550.
- Vanderbrug, G. J., 1976. Line Detection in Satellite Imagery. *IEEE Transactions on Geoscience Electronics*. 1, 37-44
- Wang, j. and Howarth, P.J., 1990. Use of the Hough Transform in Automated Lineament Detection. *IEEE Transactions on Geoscience and Remote Sensing*. 28 (4), 561-566.
- Wernicke, B. and Burchfield, B.C., 1982. Modes of Extensional Tectonics. *Journal of Structural Geology*. 4, 105-115.
- Westaway, R., 1994. Present-Day Kinematics Of The Middle East And Eastern Mediterranean. *J. Geophys. Res.* 99, 12071–12090.

- Westaway, R., 2004. Kinematic Consistency Between The Dead Sea Fault Zone And The Neogene And Quaternary Left-Lateral Faulting In SE Turkey. *Tectonophysics*. 391, 203-237.
- Yazgan, E. 1984. Geodynamic evolution of the Eastern Taurus Region. In: *Geology of The Taurus Belt*. Tekeli, O. and Göncüoğlu, M.C. (eds). *General Directorate of Mineral Research and Exploration (MTA) Special Publication*. 199-208.
- Yurur M. T., Chorowicz J., 1998. Recent Volcanism, Tectonics And Plate Kinematics Near The Junction Of The African, Arabian And Anatolian Plates In The Eastern Mediterranean. *Journal of Volcanology and Geothermal Research*. 85 (1), 1-15.
- Yurtmen, S., Guillou, H., Westerman, R., Rowbotham, G., Tatar, O., Rate Of Strike Slip Motion On The Amanas Fault (Karasu Valley, Southern Turkey) Constrained By K-Ar Dating And Geochemical Analysis Of Quaternary Basalts. *Tectonophysics*. 344, 207-246.
- Zlatopolsky, A. A., 1992. Program LESSA (Lineament Extraction And Stripe Statistical Analysis) Automated Linear Image Features Analysis— Experimental Results. *Computers & Geosciences*. 18 (9), 1121–1126.
- Zlatopolsky, A. A., 1997. Description of Texture Orientation in Remote Sensing Data Using Computer Program LESSA, *Computers & Geosciences*. 23 (1), 45-62.

## APPENDIX A

The local lineament map produced from aerial photographs are illustrated in Figure A.1.

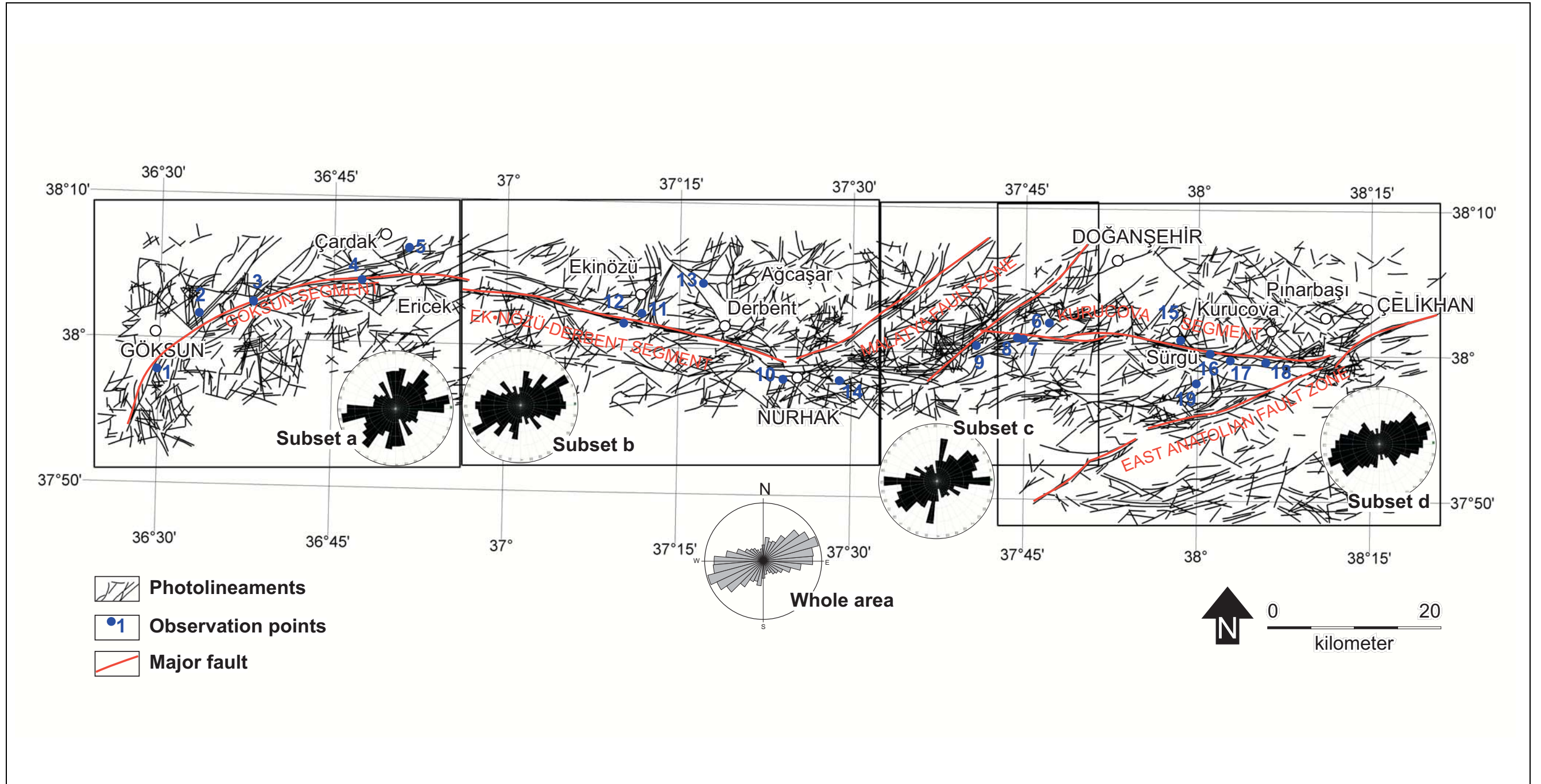


Figure A.1 Local lineament map of the Sürgü Fault Zone extracted from the aerial photographs.

## APPENDIX B: GLOSSARY

**Alluvial Fan:** n. A fan-shaped deposit of sand, mud, etc. formed by a stream where its velocity has slowed, such as at the mouth of a ravine or at the foot of a mountain.

**Cataclasite:** A rock, such as tectonic breccia, containing angular fragments that have been produced by the crushing and fracturing of preexisting rocks as a result of mechanical forces in the crust. Its fabric is a structureless rock powder.

**Conjugate Fault Pairs:** Describes a pair of intersecting (or nearly intersecting) faults, the slip motions of which are opposite (e.g., right-lateral and left-lateral), so as to accommodate the rotation of the block they bound. Conjugate faults will sometimes slip roughly "simultaneously" (within hours or days of each other), causing pairs of earthquakes.

**Dextral fault:** Right-lateral strike slip fault.

**En-echelon:** Said of the geological features that are in an overlapping or staggered arrangement, e.g. faults. Each is relatively short but collectively they form a linear zone, in which the strike of the individual features is oblique to that of the zones as a whole.

**Fault Breccia:** A tectonic breccia composed of angular fragments resulting from the crushing, shattering, or shearing of rocks during movements on a fault.

**Fault Gauge:** Soft, uncemented pulverized clayey or claylike material, commonly a mixture of minerals in finely divided form, found along some faults or between the walls of a fault, and filling or partly filling a fault zone.

**Holocene:** An epoch of the Quaternary period from, the end of the Pleistocene, approximately 8 thousand years ago to the present time: corresponding series of rocks and deposits.

**Juxtaposition:** Juxtaposition is placing things (such as lithologies in geology) side-by-side.

**Phacoid:** A frequently used term for a lenticular metamorphic structure.

**Pleistocene:** An epoch of the Quaternary period, after the Pliocene and before Holocene. It began two to three million years ago.

**Pressure Ridge:** A ridge has elongated shape and produced by transverse pressure and shortening of the land surface.

**Sag Ponds:** A small body of water occupying an enclosed depression or sag-formed where active or recent fault movement has impounded drainage.

**Sinistral:** Left-lateral strike slip fault.

**Slickenside:** A polished and smoothly striated surface that results from friction along a fault plane.

**Shutter Ridge:** A ridge formed by vertical, lateral or oblique displacement on a fault traversing a ridge and valley topography, with the displaced part of a ridge "shutting in" the adjacent ravine or canyon.

**Terrace:** Terrace produced by the more rapid erosion of weaker strata lying on more resistant rocks in a formation with horizontal bedding.